# On the acoustic field in a Pekeris waveguide with attenuation in the bottom half-space

Michael J. Buckingham[a] and Eric M. Giddens
*Marine Physical Laboratory, Scripps Institution of Oceanography, University of California—San Diego, 9500 Gilman Drive, La Jolla, California 92093-0238*

(Received 4 April 2005; revised 1 November 2005; accepted 2 November 2005)

The acoustic field in a Pekeris channel with an attenuating basement is critically examined, based on contour integrations of the wave number integrals for the two domains. In both regions, the field consists of a finite sum of proper (square integrable) normal modes plus a branch line integral around a hyperbolic cut. For low bottom attenuation, only "trapped" modes exist but as the loss increases additional "dissipation" modes contribute to the mode sum. A Newton-Raphson iterative procedure is introduced for finding the complex eigenvalues of the modes and a new expression is derived which shows that the total number of proper (trapped plus dissipation) modes supported by the waveguide increases essentially linearly with rising bottom attenuation. Approximations for the complex shape functions of the modes in the water column and the basement are developed and compared with the exact shape functions determined from the Newton-Raphson procedure. An expression derived for the modal attenuation coefficient scales in proportion to the square of the mode number and inversely with the square of the frequency. Stationary-phase approximations for the branch line integrals for both domains are developed, which serve to illustrate the asymptotic range dependence of the lateral wave but otherwise have little utility. © *2006 Acoustical Society of America.* [DOI: 10.1121/1.2141212]

PACS number(s): 43.30.Bp, 43.20.Bi [AIT] Pages: 123–142

## I. INTRODUCTION

A solution of the wave equation for the sound field in an iso-speed ocean channel overlying a homogeneous fluid half-space was developed and published over half a century ago in a classic paper by Pekeris.[1] His solution for the acoustic pressure consists of a sum of normal modes plus a branch line integral, the latter originating in the so-called Pekeris branch cut, which runs vertically in the complex-wave-number plane, parallel to the imaginary axis. Pekeris was careful not to specify how many modes are included in his mode sum, although he did make it clear that, because of the density discontinuity at the bottom interface, the modes are not orthogonal over either the water column or the entire fluid domain. As for the branch-line integral, Pekeris was vague about its physical interpretation.

Over 25 years later, in describing the Pekeris solution, Stickler[2] stated that it consists of three components: a finite sum of $M$ "proper" modes, each of which decays exponentially with depth in the basement and hence is convergent (i.e., square integrable); an infinite sum of "improper" modes, each of which is divergent, growing exponentially with depth in the basement; and a contribution from the contour integration around the vertical branch cut. The presence of the unphysical improper modes is noteworthy because, by diverging to infinity in the basement, they violate one of the radiation conditions upon which Pekeris predicated his analysis. It should be appreciated, however, that Pekeris[1] himself made no reference to diverging modes in the basement.

An alternative to the Pekeris solution, also described by Stickler,[2] is based on a hyperbolic branch line that is attributed to Ewing, Jardetzky, and Press[3] and commonly referred to as the EJP cut. In this case, the solution consists of two components, a finite sum of $M$ normal modes (identical to the proper modes in the Pekeris solution) plus a branch line integral taken around the EJP branch line. Both the mode sum and the EJP branch line integral are well behaved in that they approach zero asymptotically in the limit of infinite depth in the basement. The EJP branch-line integral represents two physically identifiable components of the acoustic field: the lateral or head wave, which propagates along the interface between the channel and the fluid basement, reradiating energy into the water column at the critical angle as it progresses, and the continuous field, which, in shallow water, penetrates through the bottom boundary into the basement and is thus lost to the water column.

In the absence of loss in the basement, the number, $M_o$, of proper normal modes obtained with either the Pekeris or EJP cut is readily determined[4] from the Pekeris dispersion relation.[1] The criterion used in deriving $M_o$ is the geometrical condition that the grazing angle of the highest-order modal equivalent ray be no greater than the critical grazing angle of the bottom interface (assuming the sound speed in the bottom to be greater than that in the water column). Under this constraint, all the modes up to and including mode number $M_o$ experience no loss from bottom interactions, since their equivalent rays are totally reflected (with a phase change) from the bottom boundary, and hence such modes

[a]Also affiliated to the: Institute of Sound and Vibration Research, The University, Southampton SO17 1BJ, England. Electronic mail: mjb@mpl.ucsd.edu

are said to be "trapped" in the water column. The shape functions describing the depth dependence of the trapped modes are real, showing oscillatory behavior in the channel and an exponential decay in the basement. The poles associated with the trapped modes lie on the real axis of the wave number complex plane, between $-k_2$ and $-k_1$, the (real) acoustic wave numbers in the basement and water column, respectively.

When attenuation is introduced into the basement, the acoustic wave number $k_2$ becomes complex and may be written as $k_2 - i\alpha$, where the imaginary part, $\alpha$, is the attenuation coefficient of plane waves in the bottom. The properties of the field are then modified in ways that are not immediately apparent. For instance, in the presence of a lossy bottom, the number of proper normal modes remains finite but increases to $M \geqslant M_o$. The additional, higher-order modes, with mode numbers greater than $M_o$ and less than or equal to $M$, appear solely as a result of dissipation in the semi-infinite basement. The term "dissipation" modes is introduced here to distinguish these additional modes from the more familiar trapped modes, the latter having mode numbers that are less than or equal to $M_o$. The shape functions of all $M$ modes are complex, although the imaginary part of each trapped mode remains negligibly small, whereas the real and imaginary parts of the dissipation modes are comparable. Since the trapped and dissipation modes are all proper modes, each is convergent, being square integrable over the semi-infinite depth of the channel and the basement.

In this article, in order to investigate the properties of the field in a Pekeris waveguide with a lossy basement, a brief but complete derivation of the acoustic field in the water column and the bottom half-space is developed. The analysis is based on the EJP branch cut and leads to the familiar wave-number-integral formulation of the field in both regions. The Pekeris dispersion relation emerges in the usual way from these integrals and, since it governs the properties of the modes, forms the basis of much of the remaining discussion. By definition, a proper mode is taken to be any solution of the Pekeris dispersion relation that *also satisfies the radiation condition at infinite depth in the basement*. In fact, this radiation condition dictates that the EJP cut be chosen when performing the contour integrations in the complex plane. As a corollary to this choice of branch cut, the improper modes discussed by Stickler,[2] which do not satisfy the radiation condition at infinite depth, are automatically excluded from the exact solution.

From the transcendental dispersion relation, new analytical approximations are developed for (1) the total number of proper modes, $M$, in the lossy waveguide, (2) the complex mode shape functions in the water column and in the basement, and (3) the modal attenuation coefficients. Additionally, a simple, rapidly convergent algorithm is introduced for finding the $M$ complex roots of the dispersion relation numerically. This numerical routine is useful not only for checking the analytical solutions but also as a guide to the positions of the poles in the complex plane. It shows immediately that the poles are not confined to the vertical strip of the complex plane between real $(-k_2)$ and $-k_1$, but are distributed along the lower side of the EJP branch cut. To provide a foundation for the subsequent analytical and numerical developments, the discussion begins with a standard derivation of the wave-number-integral solution for the field in the channel and the semi-infinite basement.

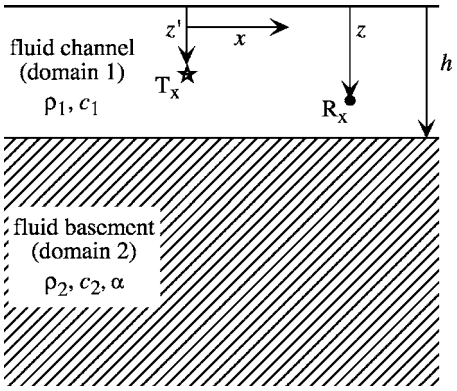


FIG. 1. The Pekeris waveguide with lossless, iso-speed channel (domain 1) overlying a homogeneous, fluid half-space (domain 2) with attenuation coefficient $\alpha$.

## II. PEKERIS WAVEGUIDE

To keep the analysis as straightforward as possible, while retaining the essential elements of the argument, a two-dimensional geometry is considered, as illustrated in Fig. 1. Cartesian coordinates are used, with $x$ and $z$, respectively, representing horizontal range and depth; the channel surface is taken to be at $z=0$ and the bottom at $z=h$. An impulsive line source normal to the plane of the diagram is at depth $z'$ in the channel and at horizontal range $x=0$. The use of Cartesian rather than the more usual cylindrical coordinates offers a minor reduction in complexity in that the horizontal range dependence of the field will be given by an exponential function instead of a Hankel function.

The wave equations to be solved for the field in the channel and the basement are

$$\frac{\partial^2 \phi_1}{\partial x^2} + \frac{\partial^2 \phi_1}{\partial z^2} - \frac{1}{c_1^2}\frac{\partial^2 \phi_1}{\partial t^2} = -Q\,\delta(z-z')\,\delta(x)\,\delta(t), \quad 0 \leqslant z \leqslant h \tag{1}$$

$$\frac{\partial^2 \phi_2}{\partial x^2} + \frac{\partial^2 \phi_2}{\partial z^2} - \frac{1}{c_2^2}\frac{\partial^2 \phi_2}{\partial t^2} = 0, \quad z > h, \tag{2}$$

where $\phi_j = \phi_j(x,z,t)$ is the velocity potential in layer $j=1$ or 2, $c_j$ are the sound speeds in the layers, $Q$ is the source strength with dimensions of (length)$^2$, $t$ is time, and $\delta(\cdot)$ is the Dirac delta function. Across the bottom boundary, the pressure and normal component of particle velocity are continuous, as expressed through the conditions

$$\rho_1 \phi_1(h) = \rho_2 \phi_2(h), \tag{3}$$

$$\phi_1'(h) = \phi_2'(h), \tag{4}$$

where $\rho_j$, $j=1,2$ are the densities in the two domains and, for convenience, the abbreviated forms $\phi_j(h) = \phi_j(x,h,t)$ and $\phi_j'(h) = [\partial \phi_j(x,z,t)/\partial z]|_{z=h}$ have been introduced. The sur-

face of the channel is taken to be a pressure-release boundary, that is, $\phi_1(0)=0$.

To solve Eqs. (1)–(4) for the field in the two domains, standard Fourier transform techniques are adopted. The temporal transform and its inverse are, respectively,

$$\phi_{j\omega} = \int_{-\infty}^{\infty} \phi_j(x,z,t)\exp(-i\omega t)dt \tag{5}$$

and

$$\phi_j(x,z,t) = \frac{1}{2\pi}\int_{-\infty}^{\infty} \phi_{j\omega}\exp(i\omega t)d\omega, \tag{6}$$

where $\omega$ is angular frequency and $i=\sqrt{-1}$. Note the use of the transform variable as a subscript to denote the transformed field, a convention which is convenient when multiple transforms are employed. Identical, bilateral transforms to those in Eqs. (5) and (6) are used in horizontal range, except that the variables are $x$ instead of $t$ and horizontal wave number $p$ in place of angular frequency $\omega$.

After transforming Eqs. (1) and (2) with respect to $x$ and $t$, they reduce to

$$\frac{\partial^2 \phi_{1\omega p}}{\partial z^2} + \eta_1^2 \phi_{1\omega p} = -Q\delta(z-z') \tag{7}$$

and

$$\frac{\partial^2 \phi_{2\omega p}}{\partial z^2} + \eta_2^2 \phi_{2\omega p} = 0, \tag{8}$$

where $k_j=\omega/c_j$, $j=1,2$, are the acoustic wave numbers in the two domains and $\eta_j$ are vertical wave numbers given by the radicals

$$\eta_1 = \sqrt{k_1^2 - p^2} \tag{9}$$

and

$$\eta_2 = \sqrt{k_2^2 - p^2}. \tag{10}$$

Implicit in Eqs. (7) and (8) are radiation conditions which require that the field and its first derivatives with respect to time and horizontal range go to zero in the limit as $|x|$ and $|t|$ go to infinity.

Equation (8) is a homogeneous second-order ordinary differential equation (ODE) whose solution may be written in the usual way as a sum of two exponentials with arguments of opposite sign. Since the radiation condition requires that the field decay to zero in the limit of infinite depth, the coefficient of the divergent exponential must be set to zero, in which case the solution is

$$\phi_{2\omega p}(z) = \phi_{2\omega p}(h)\exp[-i\eta_2(z-h)], \quad z>h. \tag{11}$$

With the sign convention chosen for the argument of the exponential in Eq. (11), the field in the basement will always decay exponentially with depth provided that

$$\mathrm{imag}(\eta_2) < 0. \tag{12}$$

As Stickler[2] recognized, this is the condition that is violated by the improper modes associated with the Pekeris cut. Equation (12) will be critically important later, when it comes to evaluating inversion integrals in the complex wavenumber plane, since it dictates the choice of branch cut.

To complete the solution for the field, a finite Fourier transform with respect to depth, $z$, is applied to Eq. (7). The finite transform is defined here as

$$\phi_{1q} = \int_0^h \phi_1(z)\exp(-iqz)dz \tag{13}$$

and standard Fourier techniques reveal its inverse to be

$$\phi_1(z) = \frac{1}{2\pi}\int_{-\infty}^{\infty} \phi_{1q}\exp(iqz)dq, \tag{14}$$

where the transform variable, $q$, is the vertical wave number. When Eq. (13) acts on the second derivative with respect to $z$, it yields, through partial integration,

$$\int_0^h \phi_1''(z)\exp(-iqz)dz = \phi_1'(h)e^{-iqh} - \phi_1'(0) + iq\phi_1(h)e^{-iqh} - q^2\phi_{1q}, \tag{15}$$

where, as in Eqs. (3) and (4), the prime on a field function denotes differentiation with respect to $z$. The integrated terms in Eq. (15) are to be determined from the boundary conditions.

On Fourier transforming Eq. (7) with respect to $z$, an algebraic equation is obtained for the triply transformed field whose solution is

$$\phi_{1\omega pq} = \frac{-Qe^{-iqz'} - \phi_{1\omega p}'(h)e^{-iqh} - iq\phi_{1\omega p}(h)e^{-iqh} + \phi_{1\omega p}'(0)}{(\eta_1^2 - q^2)}. \tag{16}$$

Since the (unknown) boundary values of the field and its derivative with respect to $z$ in this expression are independent of $q$, an inverse transform with respect to $q$ may be performed directly on Eq. (16). The integrals involved are all known forms,[5] allowing the inverse transform to be expressed explicitly. On combining the result with the boundary conditions in Eqs. (3) and (4), solutions are obtained for the unknown terms $\phi_{1\omega p}(h)$, $\phi_{2\omega p}(h)$, $\phi_{1\omega p}'(0)$, and $\phi_{1\omega p}'(h)$. Then, after performing a Fourier inversion with respect to horizontal wave number, $p$, the fields in the water column [from Eq. (16)] and the basement [from Eq. (11)] are found to be

$$\phi_{1\omega}(x,z) = \frac{Q}{2\pi}\int_{-\infty}^{\infty} F_1(\eta_1,\eta_2)e^{ipx}\,dp, \quad \text{for } 0 \leqslant z \leqslant h, \tag{17}$$

and

$$\phi_{2\omega}(x,z) = \frac{b_{12}Q}{2\pi}\int_{-\infty}^{\infty} F_2(\eta_1,\eta_2)e^{ipx}\,dp, \quad \text{for } h < z. \tag{18}$$

The two functions of $\eta_1$ and $\eta_2$ in the integrands of these inversion integrals are

$$F_1(\eta_1,\eta_2)=\frac{\sin(\eta_1 z_<)}{\eta_1}\frac{\{\eta_1\cos[\eta_1(h-z_>)]+ib_{12}\eta_2\sin[\eta_1(h-z_>)]\}}{[\eta_1\cos(\eta_1 h)+ib_{12}\eta_2\sin(\eta_1 h)]} \tag{19}$$

and

$$F_2(\eta_1,\eta_2)=\frac{\sin(\eta_1 z')e^{-i\eta_2(z-h)}}{[\eta_1\cos(\eta_1 h)+ib_{12}\eta_2\sin(\eta_1 h)]}, \tag{20}$$

where $z_>(z_<)$ is the greater (lesser) of $z$ and $z'$. Note that $F_1$ and $F_2$ are even in $\eta_1$ and mixed in $\eta_2$.

The Fourier wave-number integrals in Eqs. (17) and (18) constitute an exact solution for the two-dimensional field from a horizontal line source in the Pekeris waveguide. They are precisely analogous to the Hankel-transform solution for the three-dimensional field from a point source derived by Pekeris.[1] Mathematically, the two- and three-dimensional solutions differ only in the kernels of the integral transforms, an exponential function for the line source and a Hankel function for the point source. The functions $F_1$ and $F_2$ in Eqs. (19) and (20), which characterize the poles and branch points in the complex plane, are identical to the corresponding functions derived by Pekeris.[1] Moreover, it is clear from Eq. (20), taken in conjunction with the condition on $\eta_2$ in Eq. (12), that $F_2$ decays exponentially with depth in the basement. It follows that the total field in the basement, as given by the wave-number integral in Eq. (18), also satisfies the required radiation condition by converging to zero in the limit of infinite depth in the lower half-space.

## III. THE COMPLEX WAVE-NUMBER PLANE

By contour integration around the complex $p$ plane, the wave-number integrals in Eqs. (17) and (18) can be converted into a sum of normal modes and a branch-line integral, the latter associated with the radical $\eta_2$, defined in Eq. (10). There is no contribution from the branch cut associated with $\eta_1$ because $F_1$ and $F_2$ are even functions of $\eta_1$, as a result of which the contributions to the integral from either side of the $\eta_1$ branch cut cancel. Thus, the only branch points that need be considered in the analysis are at $p=\pm k_2$.

### A. The dispersion relation

The functions $F_1$ and $F_2$ have the same denominator:

$$D=\eta_1\cos(\eta_1 h)+ib_{12}\eta_2\sin(\eta_1 h), \tag{21}$$

which, in both cases, determines the position of the (simple) poles in the complex $p$ plane. Thus, the poles for the water column are identical to the poles for the basement, which is only to be expected since a mode is a single entity extending throughout the channel and the underlying half-space. These poles occur at the zeros of Eq. (21), that is, they are the roots of the classic dispersion relation derived by Pekeris:[1]

$$\tan(\eta_1 h)=i\frac{\eta_1}{b_{12}\eta_2}. \tag{22}$$

This equation may be expressed solely in terms of $\eta_1$ as follows:

$$\tan(\eta_1 h)=-\frac{\eta_1}{b_{12}\sqrt{k_1^2-k_2^2-\eta_1^2}}, \tag{23}$$

where, for consistency with the condition on $\eta_2$ in Eq. (12), the real part of the radical must be positive. Equation (23) can always be written in the form

$$\eta_1 h=m\pi-\tan^{-1}\left(\frac{\eta_1}{b_{12}\sqrt{k_1^2-k_2^2-\eta_1^2}}\right),\quad m=1,2,\ldots,M, \tag{24}$$

where the integer $m$ may be identified as the mode number. The modes themselves are, of course, the residues of the integrands in Eqs. (17) and (18) evaluated at the poles, $p_m$, which are the complex eigenvalues found from the solutions of Eq. (24).

Equation (24) has only a finite number of solutions that also satisfy the required inequality in Eq. (12). Thus, the set of modes is finite, with $M$ being the maximum mode number. For the special case of a lossless basement, it is clear from the form of the dispersion relation in Eq. (23) that the eigenvalues lie on the real axis between $-k_1$ and $-k_2$, but, in general, the eigenvalues are complex, appearing in the second quadrant of the complex $p$ plane. The value of $M$, along with an iterative algorithm for solving Eq. (24) numerically for the complex eigenvalues, $p_m$, will be discussed later.

Meanwhile, an approximate solution of Eq. (24) for the trapped modes is obtained by expanding the arctan function to first order in $\eta_1$:

$$\eta_1 h\approx m\pi-\frac{\eta_1 h}{b_{12}k_1\sin(\alpha_c)}, \tag{25}$$

where $\alpha_c=\cos^{-1}(k_2/k_1)$ is the critical grazing angle of the bottom interface. It is implicit here that $k_2$ is real, or nearly so, corresponding to a basement layer that exhibits negligible loss. The solution of Eq. (25) can be immediately written as

$$\eta_{1m}\approx\frac{m\pi}{h_e}, \tag{26}$$

where

$$h_e=h\left[1+\frac{1}{b_{12}k_1 h\sin(\alpha_c)}\right] \tag{27}$$

is the "effective depth" of the channel, which was originally derived by Weston[6] from an argument involving the Rayleigh reflection coefficient. To the same level of approxima-

tion as in Eq. (26), it follows from Eqs. (9) and (10) that the vertical wave number of the $m$th mode in the basement is

$$\eta_{2m} \approx -ik_1 \sin(\alpha_c)\sqrt{1-\frac{m^2\pi^2}{k_1^2 h_e^2 \sin^2(\alpha_c)}}, \tag{28}$$

and the corresponding eigenvalue is

$$p_m \approx -k_1\sqrt{1-\frac{m^2\pi^2}{k_1^2 h_e^2}}. \tag{29}$$

Physically, the effective depth in Eq. (27) expresses the idea that the phase change experienced by a modal equivalent ray undergoing total reflection from the bottom is approximately equal to the geometrical phase change from a fictitious, pressure-release boundary displaced beneath the actual interface by a distance $(h_e - h)$. Although $h_e$ depends weakly on frequency, through the presence of the acoustic wave number $k_1$, it possesses the desirable property of being independent of mode number. This has proved useful in the analyses of array performance in shallow water[7] and acoustic propagation in a three-dimensional, penetrable wedge.[8]

From the approximate expressions given above, it is apparent that the effective depth, rather than the actual depth, is the factor that controls the trapped-mode shapes in the water column [Eq. (26)], the modal decay in the basement [Eq. (28)], and the modal attenuation coefficients [from an extension of Eq. (29) to be discussed below]. On the other hand, the total number of trapped modes, $M_o$, supported by the channel is governed by the actual depth, not the effective depth.

### B. The branch cut

The vertical wave number $\eta_2$ has branch points at $p = \pm k_2$ in the complex $p$ plane, which, with the sign convention adopted here, fall in the second and fourth quadrants, as shown in Fig. 2. With $x$ positive, the contour used to evaluate the wave-number integrals in Eqs. (17) and (18) must be taken around the upper half-plane (from Cauchy's theorem and Jordan's lemma) and everywhere within that contour the imaginary part of $\eta_2$ must be negative in order to avoid violating the constraint in Eq. (12). This condition is achieved by choosing a branch cut such that the imaginary part of $\eta_2$ is negative everywhere on the top Riemann sheet, where the integration is to be performed, and positive everywhere on the bottom Riemann sheet. The appropriate branch cut is the locus of $\eta_2$ when the imaginary part is identically zero, a choice which, as discussed by Felsen and Marcuvitz,[9] yields a hyperbola in the complex $p$ plane (Fig. 2). This hyperbolic branch line is the familiar EJP cut.

### C. Normal modes and the branch line integral

By indenting the D-shaped integration contour in the upper half-plane around the EJP cut, as shown in Fig. 2, the field expressions in Eqs. (17) and (18) may be expressed as

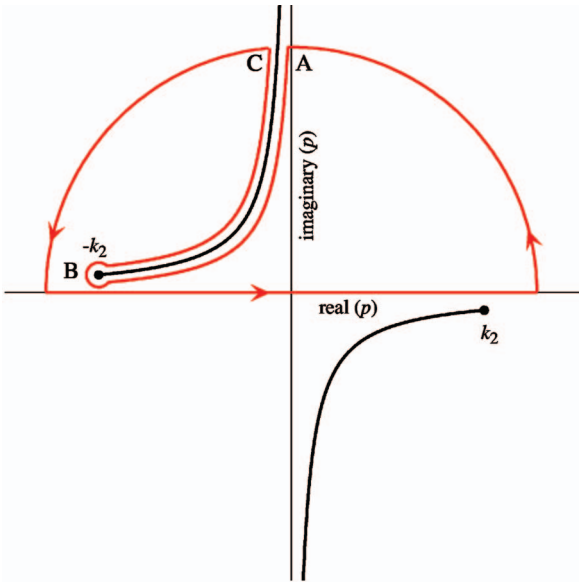


FIG. 2. Sketch of the complex $p$ plane showing branch points at $\pm k_2$ and the corresponding hyperbolic EJP branch cuts, which ensure that everywhere on the top Riemann sheet the imaginary part of $\eta_2$ is less than zero. The D contour (red line) of infinite radius in the upper half-plane is used for evaluating the wave number integrals [Eqs. (17) and (18)] for the field in the channel and the basement.

$$\phi_{1\omega}(x,z) = \frac{Q}{2\pi}\left\{2\pi i\sum_{m=1}^{M}\mathrm{Res}[F_1(\eta_{1m},\eta_{2m})e^{ip_m x}] + \oint_{\mathrm{EJP}} F_1(\eta_1,\eta_2)e^{ipx}\,dp\right\} \tag{30}$$

and

$$\phi_{2\omega}(x,z) = \frac{b_{12}Q}{2\pi}\left\{2\pi i\sum_{m=1}^{M}\mathrm{Res}[F_2(\eta_{1m},\eta_{2m})e^{ip_m x}] + \oint_{\mathrm{EJP}} F_2(\eta_1,\eta_2)e^{ipx}\,dp\right\}, \tag{31}$$

where $\eta_{1m}, \eta_{2m}$ are the vertical wave numbers evaluated at the poles.

Following the usual procedure to evaluate the residues in these expressions, the function $D$ in Eq. (21) is expanded to first order in a Taylor series about the eigenvalue $p_m$. After eliminating $\eta_{2m}$ using the dispersion relation in Eq. (22), the result is

$$\begin{aligned} D &= (p-p_m)\left.\frac{\partial D}{\partial p}\right|_{p=p_m} + \cdots \\ &= \frac{p_m}{\eta_{1m}\sin(\eta_{1m}h)}[\eta_{1m}h - \sin(\eta_{1m}h)\cos(\eta_{1m}h) \\ &\quad - b_{12}^2\sin(\eta_{1m}h)\tan(\eta_{1m}h)](p-p_m) + \cdots. \end{aligned} \tag{32}$$

Some straightforward algebra then yields the residues of these simple poles as

$$\mathrm{Res}[F_1(\eta_{1m},\eta_{2m})e^{ip_m x}] = \frac{\eta_{1m}\sin(\eta_{1m}z)\sin(\eta_{1m}z')}{p_m[\eta_{1m}h - \sin(\eta_{1m}h)\cos(\eta_{1m}h) - b_{12}^2\sin(\eta_{1m}h)\tan(\eta_{1m}h)]}e^{ip_m x} \tag{33}$$

and

$$\mathrm{Res}[F_2(\eta_{1m},\eta_{2m})e^{ip_m x}] = \frac{\eta_{1m}\sin(\eta_{1m}h)\sin(\eta_{1m}z')\exp[-i\eta_{2m}(z-h)]}{p_m[\eta_{1m}h - \sin(\eta_{1m}h)\cos(\eta_{1m}h) - b_{12}^2\sin(\eta_{1m}h)\tan(\eta_{1m}h)]}e^{ip_m x}. \tag{34}$$

The expression for the normal modes in Eq. (33) is valid for all $z$ and $z'$ in the channel, irrespective of which is the greater, and, under the constraint in Eq. (12), it is clear that the mode functions in Eq. (34) all decay to zero in the limit of infinite depth. For a wave traveling away from the source in the positive $x$ direction, the real part of the eigenvalue, $p_m$, is chosen to be negative, in which case the imaginary part is positive, as required if the modes are to attenuate with increasing distance. Notice that the residues in Eqs. (33) and (34), representing a line source, contain no geometrical decay factor, unlike the modes from a point source, which undergo cylindrical spreading, falling off as $1/\sqrt{x}$ in the far field.

The branch line integrals in Eqs. (30) and (31) are taken along the contour ABC around the EJP cut in Fig. 2. Since, by definition, $\eta_2$ is real everywhere along the EJP branch line, with phases of $-\pi$ and zero, respectively, on the upper and lower edges of the cut, a change of integration variable from $p$ to $\eta_2$ allows the branch line integrals to be converted to definite integrals over infinite limits:

$$\begin{aligned}\phi_{1\omega\mathrm{EJP}}(x,z) &= \frac{Q}{2\pi}\oint_{\mathrm{EJP}} F_1(\eta_1,\eta_2)e^{ipx}\,dp \\ &= \frac{Q}{2\pi}\int_{-\infty}^{\infty}\frac{\eta_2}{\sqrt{k_2^2-\eta_2^2}}F_1(\eta_1,\eta_2)e^{-i\sqrt{k_2^2-\eta_2^2}x}\,d\eta_2\end{aligned} \tag{35}$$

and

$$\begin{aligned}\phi_{2\omega\mathrm{EJP}}(x,z) &= \frac{Q}{2\pi}\oint_{\mathrm{EJP}} F_2(\eta_1,\eta_2)e^{ipx}\,dp \\ &= \frac{Q}{2\pi}\int_{-\infty}^{\infty}\frac{\eta_2}{\sqrt{k_2^2-\eta_2^2}}F_2(\eta_1,\eta_2)e^{-i\sqrt{k_2^2-\eta_2^2}x}\,d\eta_2,\end{aligned} \tag{36}$$

where the explicit negative sign preceding the radical in the argument of the exponential function ensures that $p = -\sqrt{k_2^2-\eta_2^2}$ falls in the second quadrant of the complex $p$ plane.

Two physically identifiable field components are represented by the branch line integrals in Eqs. (35) and (36): the lateral or head wave and the so-called continuous field. The lateral wave, discussed in Sec. VIII B, travels along the bottom interface, reradiating energy into the water column at the critical grazing angle, with an accompanying evanescent component in the basement. As the name suggests, the continuous field propagates over a continuum of grazing angles and possesses properties that depend largely on the depth of the channel relative to a wavelength. In a shallow channel with a nominally lossless bottom, the continuous field includes significant wave-number components that propagate at grazing angles steeper than the critical. Much of this high-angle energy penetrates the bottom boundary to radiate away into the basement, thus being lost to the water column. However, the partial reflections from the bottom give rise to an interference field in the water column, which may be approximated by an infinite set of "virtual" modes (see Sec. VIII C). The situation is different in deep channels, where the effect of bottom reflections on the field in the water column is negligible. In this case, the continuous field corresponds to the direct and surface-reflected arrivals at the receiver, as discussed in Sec. VIII A.

Since the solution embodied in Eqs. (30) and (31) for the total field in the Pekeris waveguide satisfies the radiation conditions in horizontal range and depth, it is well behaved everywhere. Each of the proper modes appearing in the summations spans the full vertical extent of the waveguide, that is, the water column and basement. Two criteria must be satisfied for such a mode to exist: the eigenvalue, $p_m$, must be a solution of the dispersion relation in Eq. (24) and the imaginary part of the associated vertical wave number in the basement, $\eta_{2m}$, must be negative [Eq. (12)]. Only $M$ eigenvalues satisfy these two conditions and hence no proper modes exist other than those represented by the discrete, convergent terms under the summation signs in Eqs. (30) and (31).

## IV. NUMERICAL EVALUATION OF THE EIGENVALUES

As mentioned earlier, with a lossless basement, the eigenvalues lie on the negative real axis of the complex $p$ plane, falling between the real acoustic wave numbers $-k_2$ and $-k_1$. In practice, dissipation is always present, in which case the eigenvalues become complex, migrating away from the real axis into the second quadrant of the $p$ plane. Provided the attenuation is "small," the number, $M$, of such eigenvalues remains equal to $M_o$, the same as in the lossless case. However, as the attenuation rises beyond a certain level, the trend is for the total number, $M$, of eigenvalues to increase beyond $M_o$. Various iterative techniques for solving the dispersion relation in Eq. (23) for the complex eigenvalues have been discussed by several authors,[10–12] all of which are based on variants of the effective depth in Eq. (27).

A more direct approach to solving the dispersion relation for its complex roots is introduced here, based on a straight-

forward application of the elementary Newton-Raphson algorithm.[13] By a slight modification of Eq. (24), the equation to be solved can be written as

$$f(X) = X - \left(m - \frac{1}{2}\right)\pi - \tan^{-1}[g(X)] = 0,$$

$$m = 1,2,\ldots,M, \tag{37}$$

where

$$X = \eta_1 h, \tag{38}$$

$$g(X) = b_{12}\frac{\sqrt{A^2 - X^2}}{X}, \tag{39}$$

and

$$A = \sqrt{k_1^2 - k_2^2}h. \tag{40}$$

In this formulation, bottom attenuation is accommodated by the usual device of allowing the acoustic wave number $k_2$ to be complex. The derivative of the function in Eq. (37) with respect to the complex variable $X$ is

$$f'(X) = \frac{df}{dX} = 1 + \frac{1}{X(1+g^2)}\left\{g + \frac{b_{12}^2}{g}\right\}. \tag{41}$$

If the $n$th approximation for the root is $X_n$, then an improved estimate is

$$X_{n+1} = X_n - \frac{f(X_n)}{f'(X_n)}, \tag{42}$$

which, with a starting value of $X_o = \left(m - \frac{1}{2}\right)\pi$, converges to the required complex solution for the vertical wave number, $\eta_{1m}$, of mode $m$ after just a few iterations. Once the vertical wave numbers of the modes in the water column have been determined, the eigenvalues are obtained from the expression

$$p_m = -\sqrt{k_1^2 - \eta_{1m}^2}, \quad m = 1,2,\ldots,M, \tag{43}$$

where, again, the minus sign in front of the radical indicates that the real part of $p_m$ is negative, thus placing the pole in the second quadrant of the complex $p$ plane, consistent with an outward-going, attenuating wave.

The total number of proper modes, $M$, is returned directly by the Newton-Raphson algorithm, since $M$ is identified as the mode whose vertical wave number, $\eta_2$, in the basement has the smallest (i.e., nearest to zero) negative imaginary part. When $m > M$, the Newton-Raphson algorithm still returns roots of the dispersion relation, all of which have $\mathrm{imag}(\eta_2) > 0$. This puts them on the lower Riemann sheet of the complex $p$ plane, outside the integration contour in Fig. 2. Such roots, representing improper modes, do not therefore contribute to the exact solution for the field in Eqs. (30) and (31).

As a check on the complex-root-finding procedure in Eq. (42), the Newton-Raphson iteration was performed for the Zhang and Tindle[12] channel ($h = 54$ m, $c_1 = 1500$ m/s, $c_2 = 1600$ m/s, $b_{12} = 0.8$) using their seabed attenuation of 0.3125 dB/m/kHz. At their frequency of $f = 100$ Hz, only three proper modes are supported, that is, $M = 3$, with complex eigenvalues, as returned by the Newton-Raphson algorithm in Eq. (42), that are identical to those shown for the first three modes in Zhang and Tindle's Table I.

The eigenvalues for modes $m = 4$, 5, and 6 that appear in Zhang and Tindle's Table I are also given identically by the Newton-Raphson procedure. However, these eigenvalues, corresponding to mode numbers $m > M$, represent improper modes with vertical wave numbers in the basement having a positive imaginary part. Thus, these improper modes, which are not part of the solution for the field in Eqs. (30) and (31), exhibit exponentially diverging oscillations with increasing depth in the basement, of the type illustrated in Fig. 5.8 of Jensen *et al.*[14]

## V. MODE COUNTING

### A. Lossless basement

With a lossless basement, since there can be no dissipation modes, only the trapped modes exist in the Pekeris waveguide, the total number being $M_o$. A well-known analytical expression[4] exists for $M_o$, which is derived from the dispersion relation in Eq. (24) under the condition that the largest mode number occurs when $\eta_1 = \sqrt{k_1^2 - k_2^2}$. The arctan function then equals $\pi/2$. Physically, this cutoff condition corresponds to the situation where the modal equivalent ray is at the critical grazing angle, in which case the bottom acts as an acoustically rigid interface. The number of trapped modes is immediately found to be

$$M_o = \frac{k_1 h}{\pi}\sin(\alpha_c) + \frac{1}{2}, \tag{44}$$

where $\alpha_c = \cos^{-1}(c_1/c_2)$ is the critical grazing angle of the interface and, since $M_o$ is a whole number, it is implicit in Eq. (44) that the right side is to be rounded down to the nearest integer. At a frequency of 200 Hz, Eq. (44) yields $M_o = 5$ for Zhang and Tindle's channel[12] with no bottom loss. When their attenuation of 0.3125 dB/m/kHz is taken into account, the total number of modes increases to $M = 7$ [evaluated from the Newton-Raphson procedure in Eq. (42)], that is, five trapped modes and two dissipation modes. As frequency increases, the number of dissipation modes rises rapidly. Evidently, in a typical shallow-water environment, over a commonly used frequency band, attenuation in the basement significantly increases the number of proper modes supported by the waveguide.

### B. Lossy basement

In general, attenuation in the basement increases the total number of proper modes to $M \geqslant M_o$, although it is considerably more difficult to derive an analytical expression for $M$ than for $M_o$. For the moment, falling back on the Newton-Raphson procedure in Eq. (42), it is found that for bottom attenuations of one, two, five, and ten times that used by Zhang and Tindle[12] in their Table I, with all else the same, including their frequency of 100 Hz, the corresponding proper mode counts are $M = 3$, 4, 7, and 12 (cf. $M_o = 3$ trapped modes). Figure 3 shows the positions of all the eigenvalues in the complex $p$ plane for these four levels of attenuation at 100 Hz in the Zhang and Tindle channel. The

TABLE I. Mode properties at $f=100$ Hz for the Zhang and Tindle channel, from the Newton-Raphson algorithm [Eq. (42)]. The letters in the first column denote bottom attenuation: $A=0.3125$, $B=0.625$, $C=0.9375$, $D=1.25$ dB/m/kHz. Mode numbers 4 and higher are dissipation modes.

| $\alpha$ | $m$ | $p_m$ | $\eta_{2m}$ | $\alpha_m$ (dB/m) |
|---|---|---|---|---|
| A | 1 | −0.415 853 5+0.000 054 7$i$ | 0.010 128 5−0.137 248 1$i$ | 0.000 475 |
| A | 2 | −0.406 681 2+0.000 239 2$i$ | 0.012 352 5−0.106 501 2$i$ | 0.002 078 |
| A | 3 | −0.391 841 2+0.001 321 5$i$ | 0.035 848 7−0.024 966 6$i$ | 0.011 479 |
| B | 1 | −0.415 839 2+0.000 106 4$i$ | 0.020 091 5−0.138 438 2$i$ | 0.000 925 |
| B | 2 | −0.406 613 3+0.000 462 4$i$ | 0.024 318 0−0.108 465 4$i$ | 0.004 017 |
| B | 3 | −0.391 211 1+0.001 870 2$i$ | 0.052 215 7−0.040 103 7$i$ | 0.016 245 |
| B | 4 | −0.365 643 4+0.006 496 3$i$ | 0.143 240 2−0.003 144 0$i$ | 0.056 426 |
| C | 1 | −0.415 759 7+0.000 226 5$i$ | 0.047 810 8−0.145 784 1$i$ | 0.001 968 |
| C | 2 | −0.406 256 2+0.000 956 8$i$ | 0.055 870 9−0.119 481 3$i$ | 0.008 311 |
| C | 3 | −0.389 833 8+0.002 712 0$i$ | 0.083 944 5−0.071 559 3$i$ | 0.023 556 |
| C | 4 | −0.364 025 6+0.006 528 3$i$ | 0.149 659 9−0.031 322 8$i$ | 0.056 704 |
| C | 5 | −0.325 411 9+0.011 754 5$i$ | 0.219 889 2−0.014 731 0$i$ | 0.102 098 |
| C | 6 | −0.269 242 6+0.019 399 4$i$ | 0.286 033 5−0.006 436 6$i$ | 0.168 501 |
| C | 7 | −0.181 554 0+0.036 212 9$i$ | 0.349 629 0−0.001 400 5$i$ | 0.314 542 |
| D | 1 | −0.415 607 1+0.000 312 7$i$ | 0.085 107 0−0.164 481 7$i$ | 0.002 716 |
| D | 2 | −0.405 619 9+0.001 288 7$i$ | 0.094 805 5−0.143 512 3$i$ | 0.011 194 |
| D | 3 | −0.388 269 5+0.003 166 2$i$ | 0.118 458 5−0.108 891 8$i$ | 0.027 501 |
| D | 4 | −0.361 832 5+0.006 463 4$i$ | 0.164 790 1−0.071 544 4$i$ | 0.056 141 |
| D | 5 | −0.323 101 3+0.011 432 7$i$ | 0.225 383 7−0.046 296 9$i$ | 0.099 303 |
| D | 6 | −0.266 693 9+0.019 067 9$i$ | 0.288 339 7−0.031 363 0$i$ | 0.165 622 |
| D | 7 | −0.178 137 4+0.036 215 8$i$ | 0.350 679 4−0.021 892 0$i$ | 0.314 567 |
| D | 8 | −0.055 333 3+0.140 697 0$i$ | 0.412 175 8−0.015 389 7$i$ | 1.222 078 |
| D | 9 | −0.033 917 4+0.268 035 6$i$ | 0.472 995 0−0.010 650 1$i$ | 2.328 127 |
| D | 10 | −0.028 526 8+0.363 678 9$i$ | 0.533 306 9−0.007 038 9$i$ | 3.158 875 |
| D | 11 | −0.026 050 5+0.446 850 4$i$ | 0.593 238 9−0.004 193 6$i$ | 3.881 293 |
| D | 12 | −0.024 633 9+0.523 392 7$i$ | 0.652 881 9−0.001 892 1$i$ | 4.546 131 |

numerical values of the poles depicted in the four panels of Fig. 3, the corresponding vertical wave numbers in the basement, and the associated modal attenuation coefficients are listed in Table I.

It is also found form Eq. (42) that, as the frequency increases, with the bottom attenuation fixed, the proper-mode count, $M$, rises more rapidly than $M_o$. For example, for frequencies of 100, 200, and 500 Hz in the Zhang and Tindle[12] channel, with their bottom attenuation of 0.3125 dB/m/kHz, the corresponding proper mode counts are $M=3$, 7, and 32 (cf. $M_o=3$, 5 and 13 trapped modes).

Apart from the fact that the number of poles increases with rising levels of dissipation and increasing frequency, it is immediately apparent from Fig. 3 that the poles are not confined to the vertical strip between real$(-k_2)$ and $(-k_1)$. Indeed, with the higher levels of attenuation, most of the poles lie well beyond this strip, tending to track the lower side of the EJP branch cut. It is also evident that, as the attenuation rises, the shape of the branch line changes, although it always follows a hyperbolic trajectory passing through the branch point at $-k_2$.

As derived below, an analytical approximation for the total number of modes in the Pekeris waveguide with attenuation in the basement is

$$M \approx \left[1 - \frac{\gamma^2 \cot^4(\alpha_c)}{R^4}\right] \frac{R k_1 h \sin(\alpha_c)}{\pi} + \frac{1}{2}, \tag{45a}$$

where

$$R = \sqrt{1 + \gamma^2 \cot^2(\alpha_c) \left\{1 + \left(\frac{k_1 h \cos(\alpha_c)}{\tanh^{-1}(b_{12})}\right)^2\right\}} \tag{45b}$$

and $\gamma$ is the loss tangent in the basement (defined below). As before, $\alpha_c=\cos^{-1}(c_1/c_2)$ is the critical grazing angle of the bottom interface and the value of $M$ returned by Eq. (45a) is to be rounded down to the nearest integer. Notice that when $\gamma$ goes to zero, representing an absence of attenuation in the basement, the expression for $M$ in Eq. (45a) reduces correctly to $M_o$ in Eq. (44). Note also that $M$ depends on the density ratio $b_{12}$, which appears in the expression for $R$ in Eq. (45b), whereas $M_o$ is independent of density.

Although an approximation, Eq. (45a) is surprisingly accurate, predicting a mode count that is either the same as the exact result returned by the Newton-Raphson procedure in Eq. (42) or differs from it by at most one. When this difference occurs, it is a consequence of the discrete nature of the process: $M$ increments by unity at combinations of the pa-

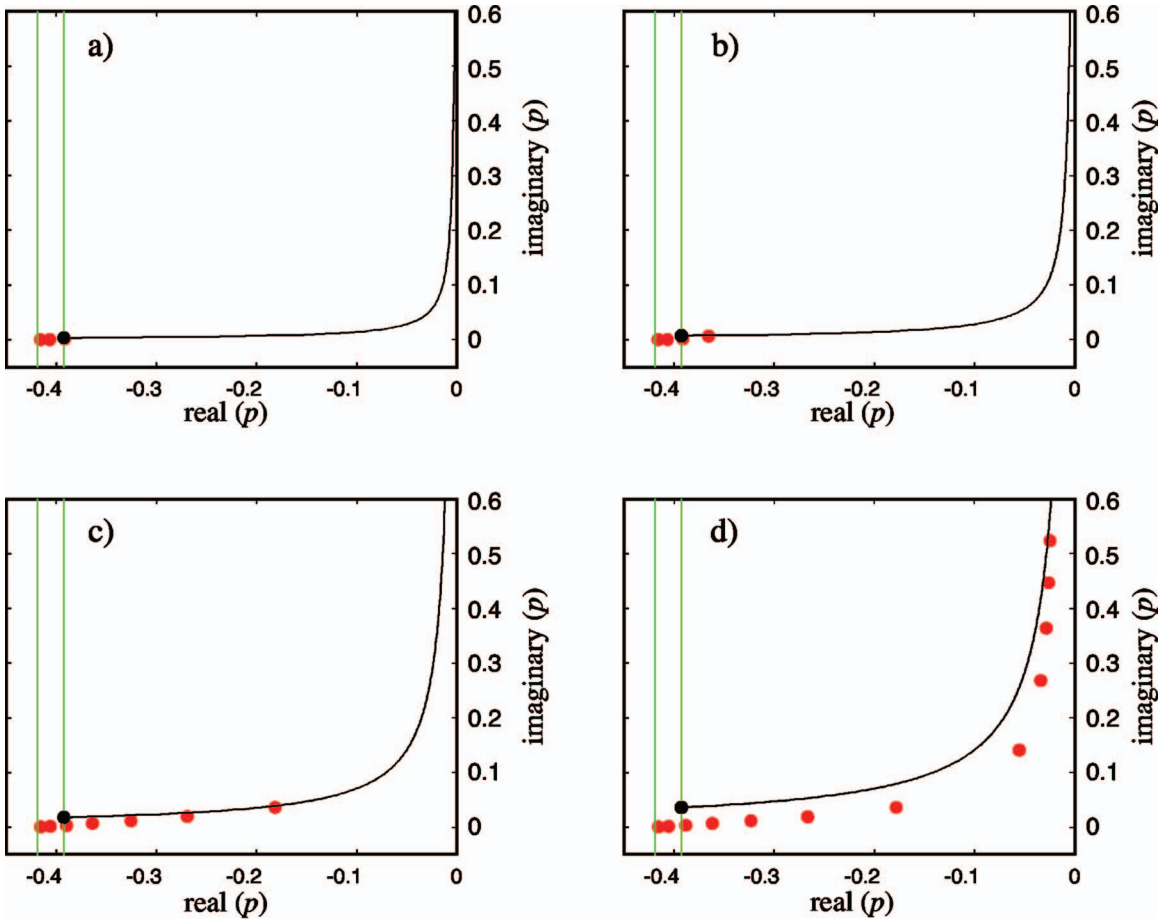


FIG. 3. Second quadrant of the complex $p$ plane showing the branch point at $-k_2$ (black circle), the hyperbolic EJP branch cut (black line), the boundaries of the strip between the real parts of $-k_1$ and $-k_2$ (green vertical lines) and the poles (red circles), as returned by the Newton-Raphson algorithm in Eq. (42), under increasing levels of bottom attenuation (which is taken to scale linearly with the frequency): (a) 0.3125 dB/m/kHz, (b) 0.625 dB/m/kHz, (c) 1.5625 dB/m/kHz, and (d) 3.125 dB/m/kHz. The remaining parameters used in the computation were those of the Zhang and Tindle channel: $h=54$ m, $c_1=1500$ m/s, $c_2=1600$ m/s, $b_{12}=0.8$, and $f=100$ Hz.

rameter values (notably attenuation and frequency) which may differ marginally between the exact and approximate calculations of the total mode number.

The derivation of Eq. (45a) proceeds as follows. In the presence of bottom attenuation, the acoustic wave number in the basement becomes complex and may be expressed as $\bar{k}_2=k_2(1-i\gamma)$, where $k_2=\omega/c_2$ is still real. From the polar representation of $\bar{k}_2$, $\gamma$ is identified as the loss tangent (i.e., the tangent of the phase angle of the complex number $\bar{k}_2$), in terms of which the plane-wave attenuation coefficient of the basement is $\alpha=\gamma k_2$. For many marine sediments, the attenuation coefficient scales essentially linearly with the frequency, in which case $\gamma$ is independent of frequency, typically taking a value close to 0.01. On recalling Eq. (24), the dispersion relation, to be solved for $m=M$, is

$$\eta_1 h = M\pi - \tan^{-1}\left(\frac{\eta_1}{b_{12}\sqrt{k_1^2-k_2^2(1-i\gamma)^2-\eta_1^2}}\right). \tag{46}$$

To obtain the solution for $M$, the vertical wave number in the water column is expressed in terms of its real and imaginary parts:

$$\eta_1 h = w + iy. \tag{47}$$

Now, the physical condition that characterizes the $M$th mode is a zero decay of the mode amplitude with increasing depth in the basement. This criterion is satisfied by setting the imaginary part of the term under the radical in Eq. (46) to zero, which yields

$$wy = k_2^2 h^2 \gamma = k_1^2 h^2 \gamma \cos^2(\alpha_c). \tag{48}$$

The arctan function in Eq. (46) is then approximated as

$$\tan^{-1}\left(\frac{\eta_1}{b_{12}\sqrt{k_1^2-k_2^2(1-i\gamma)^2-\eta_1^2}}\right) \approx \frac{\sqrt{w^2-y^2-a^2}}{w^2+y^2}(y+iw)\tanh^{-1}(b_{12}), \tag{49}$$

where

$$a = k_1 h \sin(\alpha_c)\sqrt{1+\gamma^2\cot^2(\alpha_c)}. \tag{50}$$

On substituting Eq. (49) into Eq. (46) and equating the real and imaginary parts, the following pair of simultaneous equations in $w$, $y$ is obtained, with the highest proper-mode number, $M$, as a parameter:

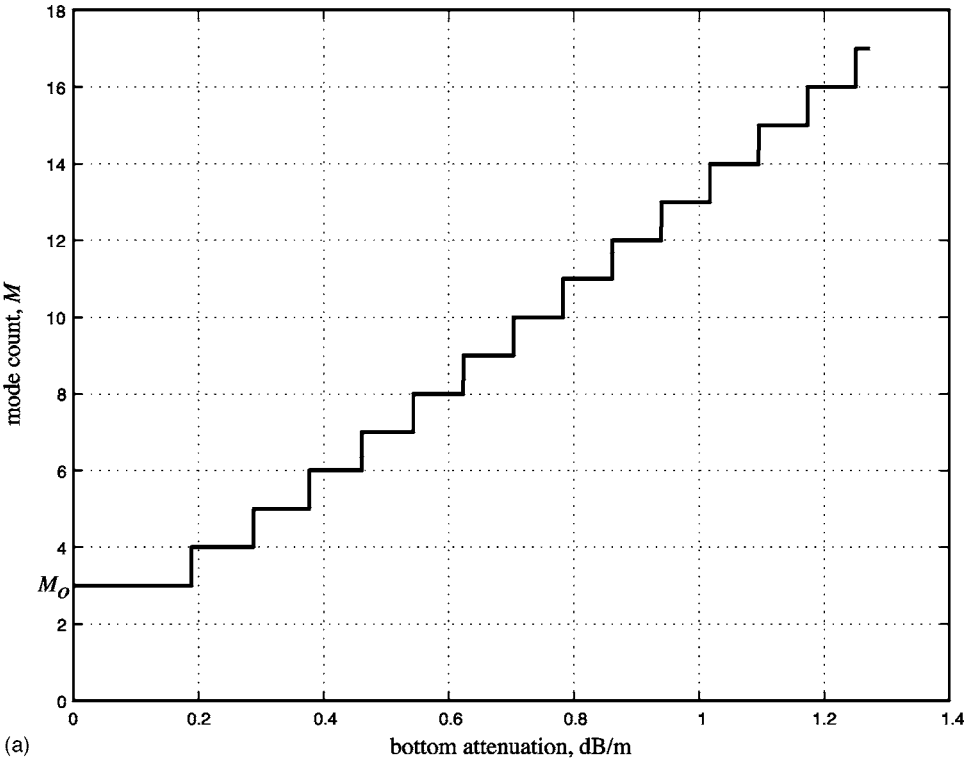


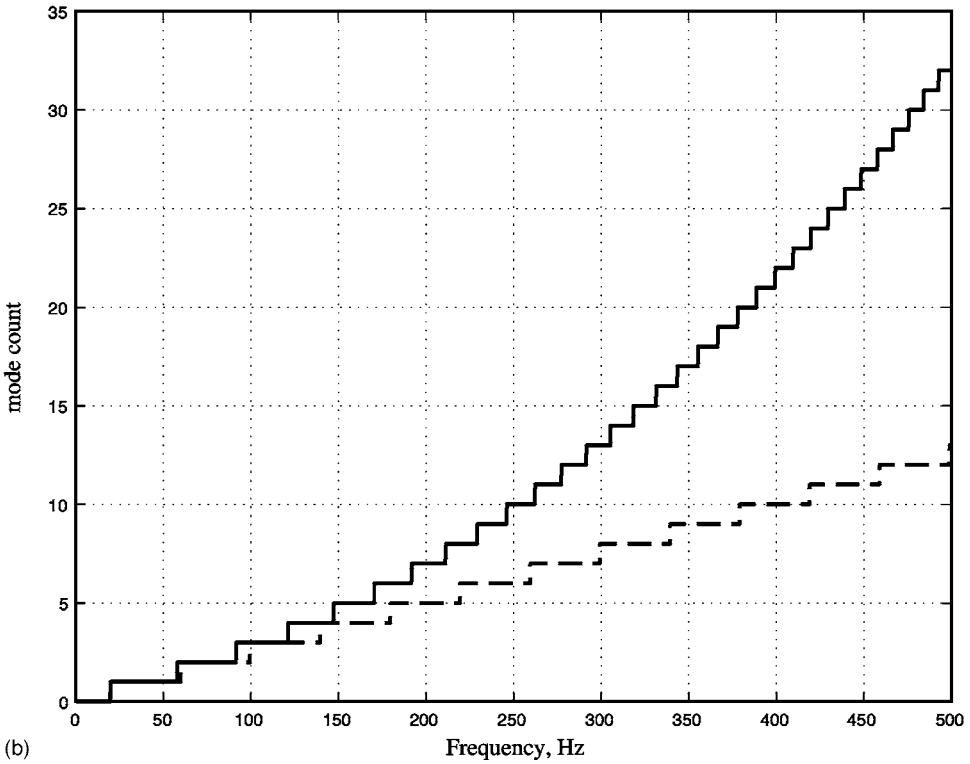


FIG. 4. (a) Mode count, $M$, evaluated from Eq. (45) as a function of the bottom attenuation at a frequency of 100 Hz and (b) $M$ [Eq. (45), solid line] and $M_o$ [Eq. (44), dashed line] as functions of frequency with a bottom attenuation of 0.3125 dB/m/kHz. The channel parameters are those of Zhang and Tindle, as cited in the legend to Fig. 3.

$$w = (M - 0.5)\pi + \frac{y\sqrt{w^2 - y^2 - a^2}}{w^2 + y^2} \tanh^{-1}(b_{12}), \tag{51}$$

$$y = \frac{w\sqrt{w^2 - y^2 - a^2}}{w^2 + y^2} \tanh^{-1}(b_{12}). \tag{52}$$

Since $y \ll w$ even for unrealistically large values of bottom attenuation, the term $y^2$ in the denominators of these expressions may be neglected, allowing $w$ to be eliminated from Eqs. (48) and (52). The result is a bi-quadratic equation in $y$, whose solution is

$$y = k_1^2 h^2 \gamma \cos^2(\alpha_c) \left\{ a^2 + \frac{k_1^4 h^4 \gamma^2 \cos^4(\alpha_c)}{[\tanh^{-1}(b_{12})]^2} \right\}^{-1/2}, \tag{53}$$

which leads to

$$w = \left\{ a^2 + \frac{k_1^4 h^4 \gamma^2 \cos^4(\alpha_c)}{[\tanh^{-1}(b_{12})]^2} \right\}^{1/2}, \tag{54}$$

and hence from Eq. (51) $M$ is found to be as given in Eq. (45a).

Figure 4(a) shows the stair-step behavior of the mode count in Eq. (45a) as a function of attenuation in the basement for the Zhang and Tindle[12] channel at a frequency of 100 Hz. Note that with an (unrealistically high) attenuation of 3.125 dB/m/kHz, the mode count from Fig. 4(a) [and also from the Newton-Raphson algorithm in Eq. (42)] is $M=12$, as shown in Fig. 3(d). Thus, in this case, in addition to the three trapped modes, there are nine dissipation modes, making 12 proper modes in total. For the same channel, but with the attenuation fixed at Zhang and Tindle's (realistic) value of 0.3125 dB/m/kHz, Fig. 4(b) shows the proper-mode count from Eq. (45a) as a function of frequency. Also shown in Fig. 4(b) for comparison is $M_o$. It is clear from this example, which is typical of many coastal ocean environments, that at commonly used frequencies, the total number of proper modes may exceed significantly the number of trapped modes. In fact, it is easy to verify many realistic combinations of waveguide parameters (i.e., channel depth, density ratio, critical angle, and bottom attenuation) and frequency return mode counts that are higher than $M_o$.

An inspection of Fig. 4(a) reveals that the trend is for the number of proper modes, $M$, to increase linearly with the attenuation, $\gamma$, in the basement. Such behavior is exhibited when the "high-loss" condition, $k_1 h \gamma \gg 1$, holds, in which case the expression for the mode count, $M$, in Eq. (45a) reduces to the simpler, linear form

$$M \approx \frac{k_1^2 h^2 \gamma \cos^2(\alpha_c)}{\pi \tanh^{-1}(b_{12})} + \frac{1}{2}. \tag{55}$$

Although not quite as accurate as Eq. (45a), Eq. (55) illustrates clearly the linear connection between the total number of proper modes, $M$, and the attenuation in the basement, $\gamma$. Obviously, since it is a high-loss approximation, Eq. (55) does not reduce to $M_o$ in the limit of zero bottom loss.

## VI. MODE SHAPE FUNCTIONS

The depth dependence of the residues for the discrete field in Eqs. (33) and (34) may be conveniently represented in terms of mode shape functions:

$$S_m(z) = \begin{cases} \sin(\eta_{1m} z), & 0 \leqslant z \leqslant h, \\ \sin(\eta_{1m} h)\exp[-i\eta_{2m}(z-h)], & z > h, \end{cases} \tag{56}$$

which is valid for all proper modes, $1 \leqslant m \leqslant M$. In the presence of bottom loss, the vertical wave number in the water column is complex and so too are the shape functions. In the case of the dissipation modes, the real and imaginary parts of each shape function have comparable amplitudes. In contrast, the vertical wave numbers of the trapped modes, $\eta_{1m}$ and $\eta_{2m}$, are essentially real and imaginary, respectively, even in the presence of high bottom loss, and hence the shape functions of the trapped modes are predominantly real with negligible imaginary parts.

### A. Trapped modes

Since the shapes of the trapped modes are insensitive to bottom loss, an approximate expression for the shape functions may be derived in terms of the (lossless) effective depth, $h_e$ [Eq. (27)]. With the aid of the expressions for the vertical wave numbers in Eqs. (26) and (28), the shape functions for $1 \leqslant m \leqslant M_o$ are

$$S_m(z) \approx \begin{cases} \sin\left(\dfrac{m\pi z}{h_e}\right), & 0 \leqslant z \leqslant h, \\ \sin\left(\dfrac{m\pi h}{h_e}\right)\exp\left[-k_1(z-h)\sin(\alpha_c)\sqrt{1-\dfrac{m^2\pi^2}{k_1^2 h_e^2 \sin^2(\alpha_c)}}\right], & z > h. \end{cases} \tag{57a}$$

The first of these expressions yields the familiar oscillatory shapes of the modes in the water column and the second returns the evanescent modal tails in the basement. The exponential decay of the latter may be characterized in terms of an e-folding depth,

$$L_m = \frac{1}{|\mathrm{imag}(\eta_{2m})|} \approx \left\{ k_1 \sin(\alpha_c)\sqrt{1-\frac{m^2\pi^2}{k_1^2 h_e^2 \sin^2(\alpha_c)}} \right\}^{-1} \quad \text{for } 1 \leqslant m \leqslant M_o. \tag{57b}$$

According to Eq. (57a), the oscillatory shapes of the trapped modes in a Pekeris channel of depth $h$ are essentially the same as those in a "perfect" waveguide with two pressure-release boundaries and of depth $h_e > h$. In the case of the Zhang and Tindle[12] channel, at their frequency of $f=100$ Hz, the effective depth from Eq. (27) is $h_e=62.6$ m, compared with the actual depth, $h=54$ m. In this case, from Eq. (57b), the approximate e-folding depths of the three trapped modes are, in order of ascending mode number, 7.3, 9.5, and 26.4 m. The corresponding e-folding depths, as evaluated "exactly" from the Newton-Raphson procedure in Eq. (42), are 7.3, 9.4, and 40.1 m. In this example, the approximation returns accurate values of the e-folding depths of the first two modes but underestimates that of mode 3. The reason for this discrepancy is that the equivalent ray of the third mode is close to the critical grazing angle, a condition under which the effective depth approximation begins to degrade.

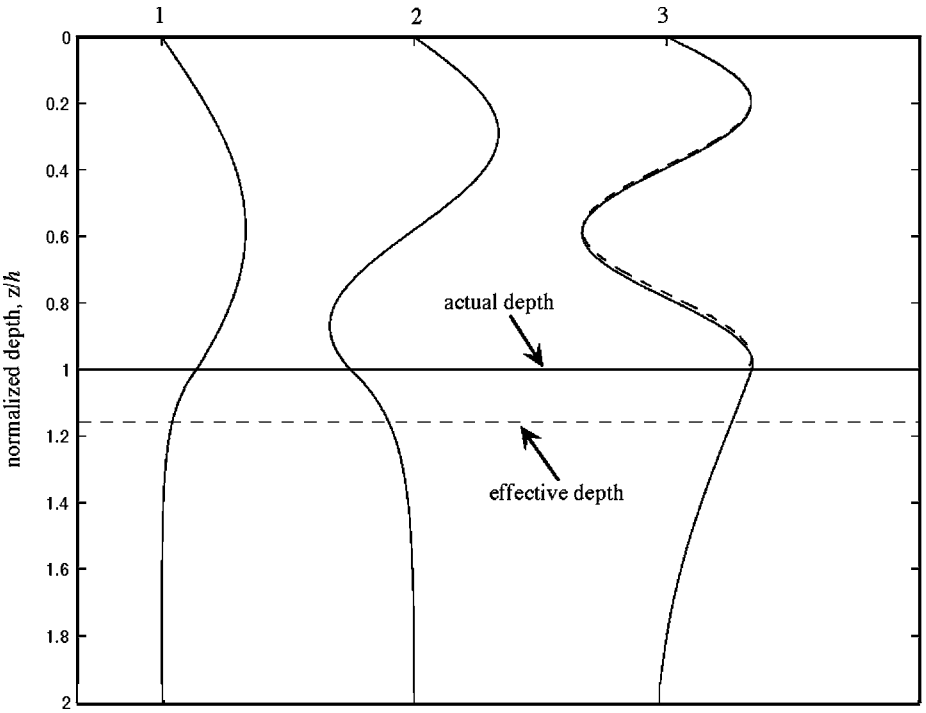


FIG. 5. Shapes of the three trapped modes in the Zhang and Tindle waveguide, as specified in Fig. 3, with a bottom attenuation of 0.3125 dB/m/kHz. The mode numbers are at the top of the panel. The solid curves were computed from the real part of the exact expression in Eq. (56), using the Newton-Raphson procedure in Eq. (42), and the dashed curves were evaluated from the approximation in Eq. (57a).

Figure 5 shows the three proper modes supported by the Zhang and Tindle[12] channel when the bottom attenuation is at their level of 0.3125 dB/m/kHz. The mode shapes were evaluated from the approximate expression in Eq. (57a) and also, for comparison, from the real part of the exact expression in Eq. (56) combined with Eq. (42). For modes 1 and 2 the approximate and exact shape functions are indistinguishable throughout the water column and basement. Even mode 3, which is very near cutoff, is quite reasonably approximated in the water column by Eq. (57a); but in the basement, the radical in Eq. (57a) is no longer real but imaginary, signifying that the approximation fails. Accordingly, in the basement, no approximate form of mode 3 is plotted in Fig. 5.

Figure 6 shows the real and imaginary parts of the seven proper modes supported by the Zhang and Tindle channel when the bottom attenuation is five times their level, at 1.625 dB/m/kHz. These mode shapes were computed using the exact expression in Eq. (56) in conjunction with Eq. (42). At this level of attenuation, four dissipation modes appear in addition to the three trapped modes, the latter exhibiting essentially the same shapes as those in Fig. 5.

### B. Dissipation modes

Dissipation modes are "leaky" in the sense that they represent partial transmissions through the bottom of the channel but they still qualify as proper modes since their eigenvalues satisfy both the dispersion relation in Eq. (24) as well as the condition in Eq. (12) on the vertical wave number in the basement. Energy leakage through the bottom occurs because the equivalent rays of the dissipation modes are steeper than the critical grazing angle. As illustrated in Fig. 6, the real and imaginary parts of the dissipation modes exhibit oscillations beneath the bottom interface, the amplitudes of which decay with increasing depth, consistent with Eq. (12). Notice that at the interface itself, both the imaginary part and the depth-gradient of the real part of the dissipation modes are essentially zero.

Approximate expressions for the shapes of the dissipation modes may be developed by introducing a slight modification to the analysis in Sec. V B for the maximum mode number $M$. When $M_o < m < M$, the condition in Eq. (48) no longer holds but, with $M$ replaced by $m$, Eqs. (51) and (52) remain valid. Expanding these two expressions to first order in the small quantities $y$ and $\gamma$ yields

$$\eta_{1m}h \approx \left(m - \tfrac{1}{2}\right)\pi + i \tanh^{-1}(b_{12}) \tag{58a}$$

and

$$\eta_{2m}h \approx \left(m - \frac{1}{2}\right)\pi - i\left(\frac{k_2^2 h^2 \gamma}{\left(m - \frac{1}{2}\right)\pi} - \tanh^{-1}(b_{12})\right). \tag{58b}$$

Taken in conjunction with Eq. (56), these expressions give rise to the following approximate forms for the shape functions of the dissipation modes:

$$S_m(z) \approx \sin\left[\left(m - \frac{1}{2}\right)\frac{\pi z}{h}\right]\cosh\left[\frac{z}{h}\tanh^{-1}(b_{12})\right] + i\cos\left[\left(m - \frac{1}{2}\right)\frac{\pi z}{h}\right]\sinh\left[\frac{z}{h}\tanh^{-1}(b_{12})\right], \quad 0 \leqslant z \leqslant h, \tag{59a}$$

and

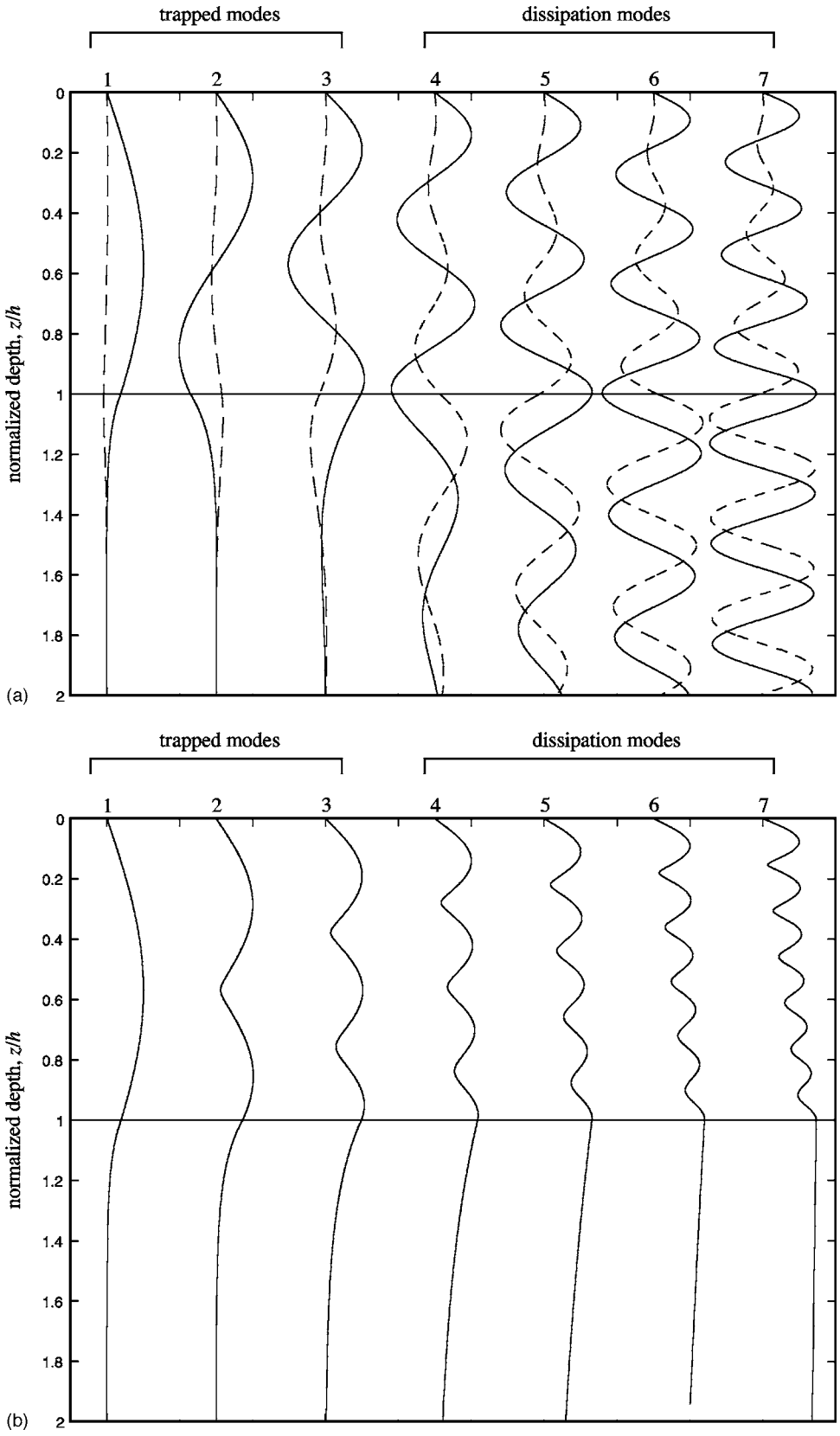


FIG. 6. Numerical evaluation of the complex mode shapes in the Zhang and Tindle waveguide, with the bottom attenuation set at 1.625 dB/m/kHz and the remaining parameters as specified in Fig. 3. The vertical wave numbers were computed from the Newton-Raphson algorithm in Eq. (42) and the mode shapes then evaluated from Eq. (56). The horizontal solid line represents the bottom of the water column and the modes are identified by the numbers at the top of the panels. (a) The real (solid curve) and imaginary (dashed curve) parts of the mode shape functions and (b) the modal envelopes.

$$S_m(z) \approx (-1)^{m+1} \cosh[\tanh^{-1}(b_{12})] \times \exp\left\{-\left[\frac{k_2^2 h^2 \gamma}{\left(m-\frac{1}{2}\right)\pi} - \tanh^{-1}(b_{12})\right]\frac{(z-h)}{h}\right\} \times \left\{\cos\left[\left(m-\frac{1}{2}\right)\frac{\pi(z-h)}{h}\right] - i\sin\left[\left(m-\frac{1}{2}\right)\frac{\pi(z-h)}{h}\right]\right\}, \quad z > h. \tag{59b}$$

According to Eq. (59a), both the imaginary part of the shape functions and the normal gradient of the real part are zero at the bottom interface, in agreement with the exact mode shapes shown in Fig. 6. The exponentially decaying oscillations in the basement, as represented by Eq. (59b), are also consistent with the exact shapes of the dissipation modes shown in Fig. 6.

The approximations leading to Eqs. (59a) and (59b) are valid under the same high-loss condition, $k_1 h\gamma \gg 1$, that underlies the approximate expression for the mode count, $M$, in Eq. (55). Indeed, Eq. (55) is recovered identically from Eq. (59b) by setting the argument of the exponential decay term to zero, which is the condition that characterizes the $M$th proper mode.

## VII. MODAL ATTENUATION

From the expressions for the residues in Eqs. (33) and (34), it is evident that if the imaginary parts of the eigenvalues are greater than zero, the modes will be attenuated as they propagate horizontally through the Pekeris waveguide. In the absence of loss in the basement, the eigenvalues are real and hence no such lateral decay occurs, but in general the modal attenuation coefficient is nonzero and given by

$$\alpha_m = \mathrm{imag}(p_m). \tag{60}$$

As shown below, the modal attenuation increases essentially as the square of the mode number and inversely as the square of the frequency. Thus, at a fixed frequency, higher-order modes are effectively removed from the field at shorter ranges, a phenomenon known as mode stripping. A given mode, on the other hand, experiences a rapid reduction in attenuation as the frequency rises, which enhances propagation to longer ranges.

### A. Mode stripping

An approximate solution for $\alpha_m$ is obtained from the dispersion relation in Eq. (46) with the arctan function represented by the first term in its Taylor expansion:

$$\eta_1 h \approx m\pi - \left(\frac{\eta_1}{b_{12}\sqrt{k_1^2 - k_2^2(1-i\gamma)^2 - \eta_1^2}}\right). \tag{61}$$

On solving for $\eta_1$ and retaining only terms up to first order in both $\eta_1$ and the small loss tangent, $\gamma$, the following expression is obtained:

$$\eta_{1m} \approx \frac{m\pi}{h_e}\left[1 + i\gamma\frac{\cot^2(\alpha_c)}{b_{12}k_1 h_e \sin(\alpha_c)}\right]. \tag{62}$$

The real part of this result is the lowest-order approximation for the vertical wave number in the water column, which has already been presented in Eq. (26).

To first order in $\gamma$, the $m$th eigenvalue is

$$p_m = -\sqrt{k_1^2 - \eta_{1m}^2} \approx -\sqrt{k_1^2 - \frac{m^2\pi^2}{h_e^2}} + i\gamma\frac{m^2\pi^2\cos^2(\alpha_c)}{b_{12}k_1^2 h_e^3 \sin(\alpha_c)\sqrt{1 - m^2\pi^2/k_1^2 h_e^2}} \tag{63}$$

and, hence, to the same level of approximation, the modal attenuation coefficient is

$$\alpha_m = \begin{cases} \gamma\dfrac{m^2\pi^2\cot^2(\alpha_c)}{b_{12}k_1 h_e^2 \sin(\alpha_c)\sqrt{k_1^2 h_e^2 - m^2\pi^2}} & \text{for } m < \dfrac{k_1 h_e}{\pi}, \\ \dfrac{1}{h_e}\sqrt{m^2\pi^2 - k_1^2 h_e^2} & \text{for } \dfrac{k_1 h_e}{\pi} < m \leqslant M. \end{cases} \tag{64}$$

The inclusion of the term $(m\pi)^2$ under the radical in the first of these expressions has only a minor effect on the predicted modal attenuation but it improves the approximation marginally for values of $m\pi$ close to $k_1 h$. If this term were neglected, the top expression in Eq. (64) would reduce to a form that was originally derived by Buckingham,[7] according to which the modal attenuation is proportional to the square of the mode number. This quadratic scaling with mode number had been recognized earlier by Kornhauser and Raney.[15] Assuming that the loss tangent, $\gamma$, is independent of frequency, as it is for many marine sediments,[16,17] and neglecting the weak frequency dependence of the effective depth, $h_e$, in Eq. (27), then the modal attenuation given by the top expression in Eq. (64) can be seen to scale inversely with the square of the frequency.

The approximation for the modal attenuation coefficient in Eq. (64) is surprisingly good for all the modes, as illustrated in Fig. 7 for the Zhang and Tindle[12] channel with four levels of attenuation in the basement. In this example, the upper expression in Eq. (64) applies for all three trapped modes and for dissipation modes from 4 up to and including 8, which covers all the modes shown in Figs. 7(a)–7(c), while the lower expression holds for dissipation modes 9–12, which appear only in Fig. 7(d). For comparison with the approximate predictions of Eq. (64), the exact modal attenuation coefficients, as computed using the Newton-Raphson algorithm in Eq. (42), are included in Fig. 7.

### B. High bottom loss

With the relatively low level of bottom loss in Figs. 7(a) and 7(b), the attenuation coefficient of the highest-order mode does not exceed the attenuation in the basement. In fact, provided that the loss tangent satisfies the inequality

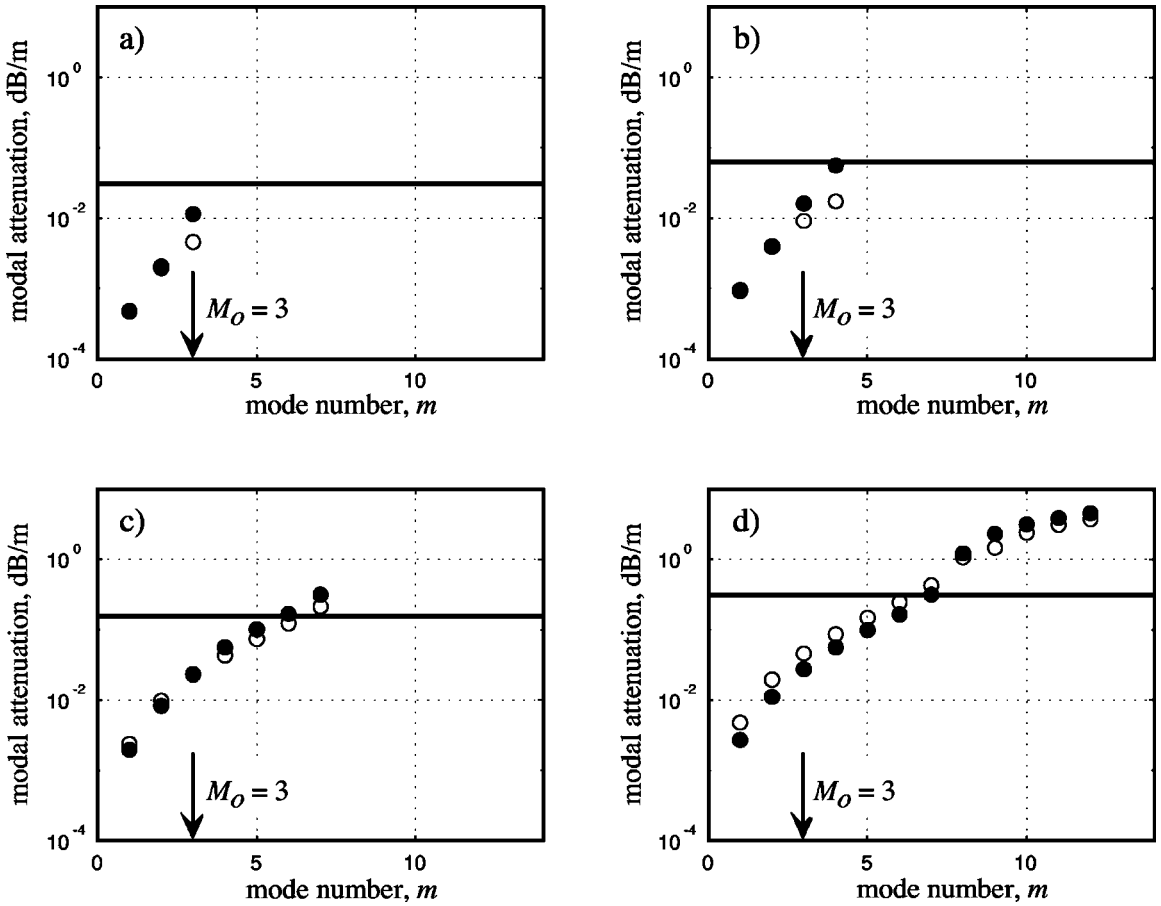


FIG. 7. Modal attenuation at 100 Hz as a function of mode number for the Zhang and Tindle channel parameters of Fig. 3 with increasing levels of attenuation in the basement: (a) 0.3125 dB/m/kHz, (b) 0.625 dB/m/kHz, (c) 1.5625 dB/m/kHz, and (d) 3.125 dB/m/kHz. The open circles derive from the approximate expression in Eq. (64) and the solid circles were computed from the "exact" Newton-Raphson algorithm in Eq. (42). The solid horizontal lines represent the plane-wave attenuation in the basement at $f=100$ Hz. The loss tangent, $\gamma$, is taken to be independent of frequency.

$$\gamma < \frac{\tanh^{-1}(b_{12})}{k_2 h}, \tag{65}$$

it is straightforward to show, from Eqs. (46) and (47) combined with the solutions for $y$ and $w$ in Eqs. (53) and (54), that the attenuation coefficient of the $M$th mode is the same as the attenuation in the bottom:

$$\alpha_M \approx \gamma k_2. \tag{66}$$

This is a familiar result with a simple interpretation based on Snell's law.

At higher levels of attenuation, Eq. (66) no longer holds, as can be seen in Figs. 7(c) and 7(d), where the attenuation coefficients of the higher-order modes exceed the attenuation in the bottom. Under the high-loss condition

$$\gamma > \frac{\tanh^{-1}(b_{12})}{k_2 h}, \tag{67}$$

it turns out that one of the second-order terms in $\gamma$ is dominant in the expression for the eigenvalue of the $M$th mode. The term in question may be identified by writing the $M$th eigenvalue in terms of $y$ and $w$, as given, respectively, in Eqs. (53) and (54):

$$\begin{aligned} p_M &= -\frac{1}{h}\sqrt{k_1^2 h^2 - \eta_{1M}^2 h^2} \\ &= -\frac{1}{h}\sqrt{k_1^2 h^2 - w^2 + y^2 - 2iwy} \\ &\approx -\frac{1}{h}\sqrt{k_2^2 h^2 - k_2^4 h^4 \gamma^2/\{\tanh^{-1}(b_{12})\}^2 - 2ik_2^2 h^2 \gamma}. \end{aligned} \tag{68}$$

When the inequality in Eq. (67) holds, the second-order term in $\gamma$ makes the real part of the term under the radical negative, in which case the attenuation coefficient may be roughly approximated as

$$\alpha_M \approx \frac{k_2^2 h \gamma}{\tanh^{-1}(b_{12})}. \tag{69}$$

This expression is greater than the attenuation in the bottom, $\gamma k_2$, by the factor $k_2 h/\tanh^{-1}(b_{12})$, which is consistent with the excess attenuation exhibited by the highest-order mode shown in Figs. 7(c) and 7(d).

### C. Observability of dissipation modes

Given the quadratic scaling of the modal attenuation with mode number [Eq. (64)], it is reasonable to ask whether dissipation modes will be too heavily attenuated to be ob-

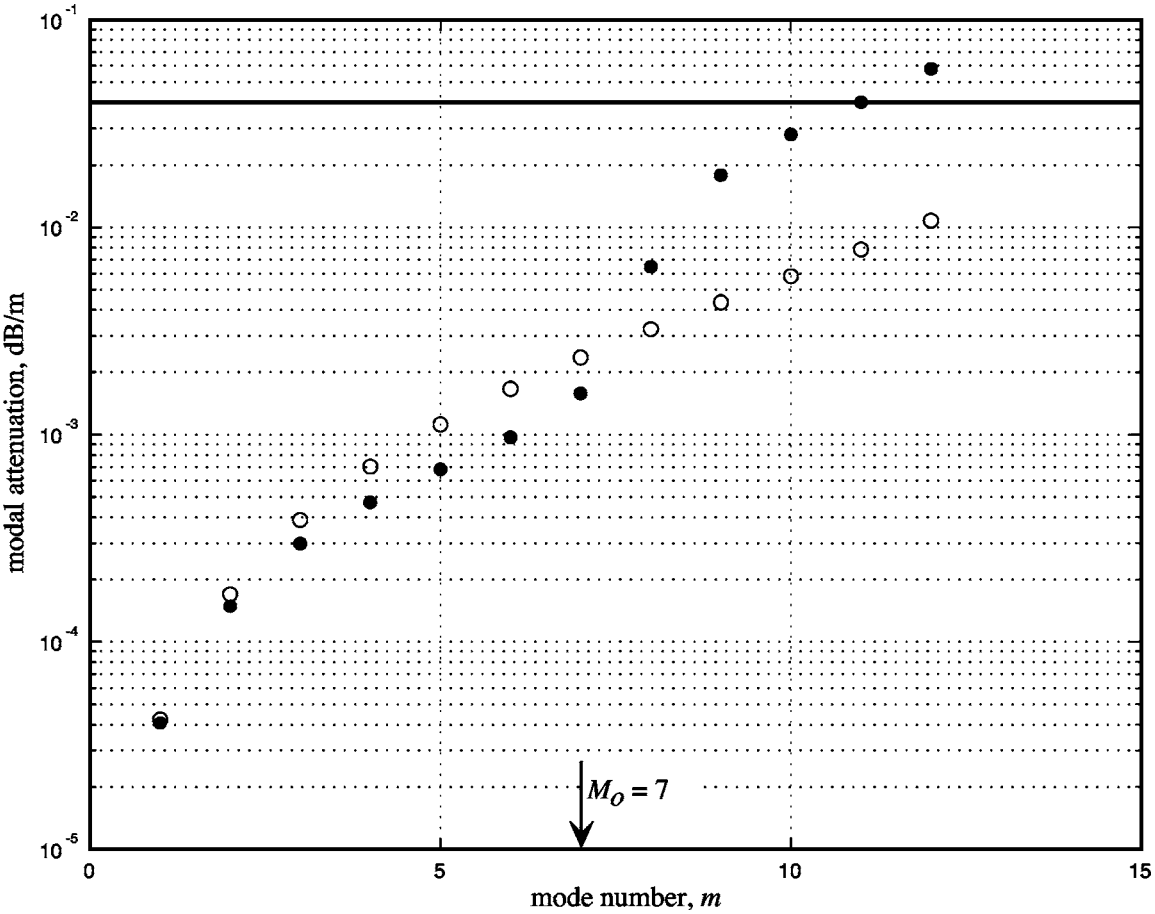


FIG. 8. Modal attenuation as a function of mode number for a frequency of 100 Hz in a 100-m channel overlying a coarse-sand sediment. See text for the bottom parameters. The open circles derive from the approximate expression in Eq. (64) and the solid circles were computed from the "exact" Newton-Raphson algorithm in Eq. (42). The solid horizontal line represents the plane-wave attenuation in the sediment at 100 Hz.

served in typical ocean channels. As an admittedly arbitrary criterion of detectability, suppose that the attenuation of the mode in question is required to be less than 10 dB over a range equal to ten times the channel depth in order to be observable. It is clear that none of the dissipation modes illustrated in Fig. 7 satisfy this condition. For instance, the first (and only) dissipation mode in Fig. 7(b) is mode 4, which is attenuated by approximately 43 dB over a range of $10h=540$ m.

However, in other circumstances that are commonly encountered in shallow ocean channels, dissipation modes which do satisfy the detectability criterion are found to exist. As an example, consider a coarse sand sediment[17] with sound speed of 1800 m/s, a density of 2.05 times the density of seawater, and an attenuation of 0.04 dB/m at 100 Hz. Assuming a channel depth $h=100$ m, a frequency of 100 Hz, and a sound speed in seawater of 1500 m/s, a total of 12 modes are supported (7 trapped and 5 dissipation modes), with attenuations as shown in Fig. 8. Mode 8, the first dissipation mode, has an attenuation $\alpha_8=0.00646$ dB/m, that is, 6.46 dB over a range of $10h=1$ km, which does indeed satisfy the detectability criterion stated above.

It is clear from the top expression in Eq. (64) that, with all else fixed, the higher the critical grazing angle of the bottom, the lower the attenuation of a given mode. Therefore, dissipation modes are most likely to be observed in channels where the sound speed in the basement is considerably higher than that in the water column, a condition that is associated with the coarser marine sediments. As illustrated in Fig. 8, at least one dissipation mode may be readily observable in an ocean channel overlying a fast sediment of coarse sand with a sound speed of 1800 m/s or higher. On the other hand, a slower, fine-grained material such as silt would not be expected to support any weakly attenuated dissipation modes. Even the very-fine-sand of the Zhang and Tindle channel, with a sound speed of 1600 m/s, is barely fast enough to support a detectable dissipation mode over a reasonable range.

## VIII. BRANCH LINE INTEGRALS

Each of the branch line integrals, Eq. (35) for the water column and Eq. (36) for the basement, represents two wave components, the head wave and the continuous field. In general, these integrals cannot be expressed explicitly. The one exception to this is the case of an infinitely deep channel, where the water-column integral reduces identically to a sum of two elementary terms, one of which represents the direct and the other the surface-reflected arrival. In shallow water, where the bottom has a significant effect on the field, the branch line integrals cannot be reduced to explicit expressions, but it is possible to develop an asymptotic approxima-

tion for the lateral wave, which is valid in both the water column and the basement. It is also possible to approximate the continuous field in the water column in terms of an infinite sum of "virtual" modes.

### A. Direct and surface-reflected arrivals in deep water

When the fluids constituting the channel and the basement are identical, that is, $b_{12}=1$, $k_1=k_2=k$, and $\eta_1=\eta_2=\eta$, the Pekeris waveguide becomes a homogeneous fluid halfspace with a pressure-release surface. The branch line integral in Eq. (35) can then be written in the form

$$\phi_{1\omega\mathrm{EJP}}(x,z)=\frac{Q}{2\pi}\int_0^\infty \frac{\eta}{\sqrt{k^2-\eta^2}}[F_1(\eta,\eta) - F_1(\eta,-\eta)]e^{-i\sqrt{k^2-\eta^2}x}\,d\eta \tag{70}$$

and, from the expression for $F_1$ in Eq. (19), it follows that

$$[F_1(\eta,\eta)-F_1(\eta,-\eta)] = -\frac{2i}{\eta}\sin(\eta z)\sin(\eta z') = \frac{i}{\eta}\{\cos[\eta(z+z')]-\cos[\eta(z-z')]\}. \tag{71}$$

By expressing each cosine as a Bessel function of the first kind, $J_{-1/2}(\cdots)$, and the exponential function in Eq. (60) as a modified Bessel function of the third kind, $K_{1/2}(\cdots)$, the branch line integral becomes

$$\phi_{1\omega\mathrm{EJP}}(x,z)=\frac{Q}{2\pi}\sqrt{\frac{x(z-z')}{\pi}}\int_0^\infty \eta^{1/2}J_{-1/2}[\eta(z-z')] \times\frac{K_{1/2}[\sqrt{\eta^2-k^2}x]}{(\eta^2-k^2)^{1/4}}\,d\eta-\frac{Q}{2\pi}\sqrt{\frac{x(z+z')}{\pi}} \times\int_0^\infty \eta^{1/2}J_{-1/2}[\eta(z +z')]\frac{K_{1/2}[\sqrt{\eta^2-k^2}x]}{(\eta^2-k^2)^{1/4}}\,d\eta. \tag{72}$$

The integrals here are special cases of Gegenbauer's discontinuous integral, which can be expressed explicitly in terms of Bessel functions,[18] yielding the following result for the branch line contribution to the field in the half space:

$$\phi_{1\omega\mathrm{EJP}}(x,z)=-\frac{iQ}{4\pi}\{H_0^{(2)}[k\sqrt{x^2+(z-z')^2}] - H_0^{(2)}[k\sqrt{x^2+(z+z')^2}]\}, \tag{73}$$

where $H_0^{(2)}(\cdots)$ are Hankel functions of the second kind of order zero.

Equation (73) is the expected result, since the first and second terms on the right represent, respectively, the field from the horizontal line source and its negative image in the pressure-release surface. The source term exhibits a logarithmic singularity at the origin, where the argument is zero; and both terms show a cylindrical-spreading type of decay at longer ranges. These properties are, of course, all characteristic of a line source.

### B. The lateral wave in shallow water

For large $x$, the asymptotic behavior of the branch line integrals in Eqs. (35) and (36) may be approximated by using the method of stationary phase.[19] The analysis is fairly standard apart from one subtlety: the stationary point of the phase function occurs at zero, which returns a null value for the integrals in Eqs. (35) and (36). This difficulty is circumvented by adopting a limiting procedure.

To illustrate the approach, consider the field in the water column when losses everywhere are negligible, in which case the acoustic wave numbers $k_1$ and $k_2$ are real. Some straightforward algebraic manipulation of the function $F_1(\eta_1,\eta_2)$ allows the integral in Eq. (35) to be written in the form

$$\phi_{1\omega\mathrm{EJP}}(x,z)=-\frac{ib_{12}Q}{2\pi}\int_{-\infty}^{\infty}\frac{\eta_2^2}{\sqrt{k_2^2-\eta_2^2}}\frac{\sin(\eta_1 z)\sin(\eta_1 z')}{[\eta_1^2\cos^2(\eta_1 h)+b_{12}^2\eta_2^2\sin^2(\eta_1 h)]}e^{-i\sqrt{k_2^2-\eta_2^2}x}\,d\eta_2, \tag{74}$$

where the negative sign in the argument of the exponential function has been written explicitly with the understanding that the real part of the radical is positive, thus ensuring that the horizontal wave number falls in the second quadrant of the complex plane. Since $\eta_1$ depends on $\eta_2$ through the expression

$$\eta_1=\sqrt{\eta_2^2+k_1^2-k_2^2}, \tag{75}$$

the integrand in Eq. (74) may expressed as a function of $\eta_2$ alone.

The quadratic multiplier in the numerator of the integrand of Eq. (74) is now written as the limit

$$\eta_2^2=i\lim_{s\to 0}\frac{d}{ds}\exp(-i\eta_2^2 s), \tag{76}$$

where $s$ is a vanishingly small dummy variable. The integral $\phi_{1\omega EJP}(x,z)$ then consists of a sum of four integrals, each of the form

$$I = \lim_{s\to 0} \frac{d}{ds} \int_{-\infty}^{\infty} \frac{\exp i\{\eta_1 Z - \sqrt{k_2^2 - \eta_2^2}x - \eta_2^2 s\}}{\sqrt{k_2^2 - \eta_2^2}[\eta_1^2 \cos^2(k_1 h) + b_{12}^2 \eta_2^2 \sin^2(k_1 h)]}\, d\eta_2, \tag{77}$$

where the four possible sign combinations are represented by $Z = \pm(z \pm z')$. Assuming that, for large $x$, the exponential in the numerator of the integrand varies much more rapidly than the denominator, the integral may be evaluated by the method of stationary phase. The phase function is

$$\theta(\eta_2) = \sqrt{\eta_2^2 + k_1^2 - k_2^2}Z - \sqrt{k_2^2 - \eta_2^2}x - \eta_2^2 s, \tag{78}$$

the first two derivatives of which are

$$\theta'(\eta_2) = \frac{\eta_2 Z}{\sqrt{\eta_2^2 + k_1^2 - k_2^2}} + \frac{\eta_2 x}{\sqrt{k_2^2 - \eta_2^2}} - 2\eta_2 s \tag{79}$$

and

$$\theta''(\eta_2) = \frac{(k_1^2 - k_2^2)Z}{(\eta_2^2 + k_1^2 - k_2^2)^{3/2}} + \frac{k_2^2 x}{(k_2^2 - \eta_2^2)^{3/2}} - 2s. \tag{80}$$

Equation (79) has a real root,

$$\eta_2 = 0, \tag{81}$$

at which point the phase function in Eq. (78) is

$$\theta(0) = \sqrt{k_1^2 - k_2^2}Z - k_2 x \tag{82}$$

and the second derivative in Eq. (80) is

$$\theta''(0) = \frac{Z}{\sqrt{k_1^2 - k_2^2}} + \frac{x}{k_2} - 2s. \tag{83}$$

The condition in Eq. (81) on the vertical wave number, $\eta_2$, is characteristic of the lateral wave, which travels horizontally through the lower medium and, in the water column, is incident on the bottom boundary at precisely the critical angle.

Since the second derivative in Eq. (83) is positive for large $x$, the turning point in Eq. (82) is a minimum, corresponding to a point of stationary phase, which yields

$$I \approx b_{12}\sqrt{2\pi}\left[\frac{1}{k_2(k_1^2 - k_2^2)\cos^2(\sqrt{k_1^2 - k_2^2}h)} \times \exp i\left\{\sqrt{k_1^2 - k_2^2}Z - k_2 x + \frac{\pi}{4}\right\}\right] \times \lim_{s\to 0} \frac{d}{ds}[\theta''(0)]^{-1/2}. \tag{84}$$

On evaluating the limit in this expression and recombining the four integrals, the asymptotic approximation for the lateral wave in the water column is found to be

$$\phi_{1\omega\text{lateral}}(x,z) \approx b_{12}Q\sqrt{\frac{\cos(\alpha_c)}{2\pi}} \frac{\sin\{k_1 z \sin(\alpha_c)\}\sin\{k_1 z' \sin(\alpha_c)\}}{(k_1 x)^{3/2}\sin^2(\alpha_c)\cos^2\{k_1 h \sin(\alpha_c\}} \times e^{-i\{k_1 x \cos(\alpha_c) - \pi/4\}}, \tag{85}$$

where $\alpha_c = \cos^{-1}(k_2/k_1)$ is the critical grazing angle. Following a similar development, the branch line integral in Eq. (36) for the lateral wave in the basement is approximated by the stationary phase expression

$$\phi_{2\omega\text{lateral}}(x,z) \approx b_{12}Q\sqrt{\frac{\cos(\alpha_c)}{2\pi}} \frac{\sin\{k_1 z' \sin(\alpha_c)\}}{(k_1 x)^{3/2}\sin^2(\alpha_c)\cos^2\{k_1 h \sin(\alpha_c)\}} \times e^{-i\{k_1 x \cos(\alpha_c) - \pi/4\}}[b_{12}\sin\{k_1 h \sin(\alpha_c)\} + k_1(z - h)\sin(\alpha_c)\cos\{k_1 h \sin(\alpha_c)\}], \tag{86}$$

where $k_1(z-h)\sin(\alpha_c)$ is taken to be small compared with unity.

Analogous expressions to those in Eqs. (85) and (86) were stated without proof by Pekeris[1] for the case of a point source. Apart from revealing that the amplitude of the lateral wave reduces rapidly with increasing range, decaying asymptotically as $x^{-3/2}$, the approximations in Eqs. (85) and (86) have little utility. Indeed, when $k_1 h \sin(\alpha_c)$ is a zero of the cosine in the denominator, it is evident that these expressions fail completely, since they diverge to infinity.

### C. Virtual modes in shallow water

In an effort to improve the efficiency of shallow-water transmission loss computations, an approximate formulation of the continuous field in the water column was developed by Tindle *et al.*[20] and subsequently extended by Tindle[21] and Stickler and Ammicht.[22] Based on a technique introduced by Labianca,[23] these authors showed that the integrand of the EJP branch line integral for the continuous field in the water column exhibits resonance peaks, which arise from partial reflections off the bottom of wave-number components that are steeper than the critical grazing angle. It is implicit in these analyses that bottom loss is negligible, in which case the channel supports $M_o$ trapped modes and no dissipation modes. By integrating over packets of wave numbers centered on the resonance peaks, Tindle *et al.*[20] approximated the branch line integral as an infinite sum of discrete "virtual" modes, each of which is oscillatory in depth with a shape function that is real and of the form

$$S_m(z) = \sin\left\{\left(m - \frac{1}{2}\right)\frac{\pi z}{h}\right\} \quad \text{for } 0 \leqslant z \leqslant h \text{ and } M_o < m \leqslant \infty. \tag{87}$$

These shape functions are the same as if the bottom were a rigid boundary.

It is perhaps worth emphasizing that virtual modes are quite distinct from dissipation modes. Virtual modes are not exact solutions of the wave equation and hence are neither "proper" nor "improper" modes. The set of *real* virtual modes is infinite with each member being a discrete *approxi-*

*mation* for the EJP branch line integral representing the continuous field, and the virtual-mode approximation holds even in the absence of bottom loss. In contrast, each of the finite set of *complex* dissipation modes represents an *exact*, convergent, discrete solution of the wave equation and such solutions exist solely because attenuation is present in the basement.

## IX. CONCLUDING REMARKS

Acoustic propagation in a Pekeris waveguide with an attenuating, semi-infinite fluid basement is critically examined in this article. The analysis hinges on familiar contour integrations around the complex wave-number plane for the field in the water column and the basement. Based on the EJP branch cut, it is argued that the exact solution for the field in both domains consists of a finite sum of proper normal modes plus a branch line integral. Both of these components of the field are well behaved in the sense that they converge to zero in the limit of infinite depth in the basement. Improper modes, with exponentially diverging tails in the basement, do not contribute to the solution.

A rapidly convergent, iterative algorithm is introduced for solving the dispersion relationship for the complex modal eigenvalues. From this numerical solution, it is demonstrated that the number of proper modes supported by the waveguide rises essentially linearly with increasing attenuation in the bottom. These proper modes comprise the familiar trapped modes and, in addition, dissipation modes that exist solely as a result of attenuation in the basement. An approximate but accurate analytical expression is derived for the total mode count [Eq. (45a)], which depends on the bottom attenuation, the ratio of densities in the water column and the basement, the water depth, and the critical angle of the bottom. The total number of proper modes predicted by this expression is almost indistinguishable from the mode count returned by the exact iterative procedure. Moreover, it is shown that for realistic combinations of the parameters, the number of proper modes supported by the waveguide may be considerably higher in the presence of bottom attenuation than in the lossless case.

The attenuation of each mode is given by the imaginary part of its eigenvalue. An approximate expression is derived for the modal attenuation coefficient [Eq. (64)], which scales with the square of the mode number. This quadratic dependence on mode number accounts for the phenomenon of mode stripping, whereby higher-order modes are effectively removed from the water column at shorter ranges than lower-order modes. Assuming a frequency-independent loss tangent for the basement layer, as is typical of many marine sediments, the modal attenuation coefficient scales inversely with the square of the frequency, indicating that as frequency rises a given mode may propagate to greater ranges. Although higher-order modes undergo increasing attenuation, dissipation modes may still be of practical significance since they could be detectable in real ocean channels, provided the bottom material has a sufficiently high sound speed. This is illustrated by an example involving an channel overlying a realistic coarse-sand sediment with a sound speed of 1800 m/s.

The depth dependence of the proper modes is described in terms of complex shape functions. In the case of trapped modes, the imaginary component of the shape function is negligible and the real part is essentially the same as in the absence of bottom loss. In contrast, the real and imaginary parts of the shape functions of the dissipation modes are comparable. Approximate expressions [Eqs. (59)] are developed for the shape functions of the dissipation modes in the water column and the basement.

The EJP branch line integrals, representing the lateral wave and the continuous spectrum in the water column and the basement, are also examined. Stationary phase approximations [Eqs. (85) and (86)] for these integrals reveal the asymptotic range dependence of the lateral wave but otherwise serve little useful purpose. Indeed, in certain cases, these asymptotic approximations for the lateral wave fail completely by diverging to infinity.

## ACKNOWLEDGMENT

This work was supported by Dr. Ellen Livingston, Ocean Acoustics Code, the Office of Naval Research, under Grant No. N00014-04-1-0063.

[1]C. L. Pekeris, "Theory of propagation of explosive sound in shallow water," in *Propagation of Sound in the Ocean*, Geological Society of America, Memoir 27 (Geological Society of America, New York, 1948), pp. 1–117.
[2]D. C. Stickler, "Normal-mode program with both the discrete and branch line contributions," J. Acoust. Soc. Am. **57**, 856–861 (1975).
[3]W. M. Ewing, W. S. Jardetzky, and F. Press, *Elastic Waves in Layered Media* (McGraw-Hill, New York, 1957).
[4]G. V. Frisk, *Ocean and Seabed Acoustics: A Theory of Wave Propagation* (Prentice-Hall, Englewood Cliffs, NJ, 1994).
[5]A. Erdélyi, *Tables of Integral Transforms, Volume 1* (McGraw-Hill, New York, 1954).
[6]D. E. Weston, "A Moiré fringe analog of sound propagation in shallow water," J. Acoust. Soc. Am. **32**, 647–654 (1960).
[7]M. J. Buckingham, "Array gain of a broadside vertical line array in shallow water," J. Acoust. Soc. Am. **65**, 148–161 (1979).
[8]M. J. Buckingham, "Theory of three-dimensional acoustic propagation in a wedge-like ocean with a penetrable bottom," J. Acoust. Soc. Am. **82**, 198–210 (1987).
[9]L. B. Felsen and N. Marcuvitz, *Radiation and Scattering of Waves* (Prentice-Hall, Englewood Cliffs, NJ, 1973).
[10]D. M. E. Chapman, P. D. Ward, and D. D. Ellis, "The effective depth of a Pekeris ocean waveguide, including shear wave effects," J. Acoust. Soc. Am. **85**, 648–653 (1989).
[11]P. Balasubramanian and M. M. Muni, "A note on "The effective depth of a Pekeris ocean waveguide, including shear effects" [Chapman *et al.*, J. Acoust. Soc. Am. **85**, 648–653 (1989)]," **88**, 564–565 (1990).
[12]Z. Y. Zhang and C. T. Tindle, "Complex effective depth of the ocean bottom," J. Acoust. Soc. Am. **93**, 205–213 (1993).
[13]R. Courant, *Differential and Integral Calculus*, 2nd ed. (Blackie & Son, London, 1937).
[14]F. B. Jensen, W. A. Kuperman, M. B. Porter, and H. Schmidt, *Computational Ocean Acoustics* (American Institute of Physics, New York, 1994).
[15]E. T. Kornhauser and W. P. Raney, "Attenuation in shallow-water propagation due to an absorbing bottom," J. Acoust. Soc. Am. **27**, 689–692 (1955).
[16]E. L. Hamilton, "Compressional-wave attenuation in marine sediments," Geophysics **37**, 620–646 (1972).
[17]M. J. Buckingham, "Compressional and shear wave properties of marine

sediments: comparisons between theory and data," J. Acoust. Soc. Am. **117**, 137–152 (2005).
[18]G. N. Watson, *A Treatise on the Theory of Bessel Functions*, 2nd ed., (Cambridge U. P., London, 1958).
[19]J. N. Newman, *Marine Hydrodynamics* (MIT, Cambridge, MA, 1977).
[20]C. T. Tindle, A. P. Stamp, and K. M. Guthrie, "Virtual modes and the surface boundary condition in underwater acoustics," J. Sound Vib. **49**, 231–240 (1976).
[21]C. T. Tindle, "Virtual modes and mode amplitudes near cutoff," J. Acoust. Soc. Am. **65**, 1423–1428 (1979).
[22]D. C. Stickler and E. Ammicht, "Uniform asymptotic evaluation of the continuous spectrum contribution for the Pekeris model," J. Acoust. Soc. Am. **67**, 2018–2024 (1980).
[23]F. M. Labianca, "Normal modes, virtual modes, and alternative representations in the theory of surface duct sound propagation," J. Acoust. Soc. Am. **53**, 1137–1147 (1973).